

1 **Title:** The structural basis of Indisulam-mediated recruitment of RBM39 to the
2 DCAF15-DDB1-DDA1 E3 ligase complex

3 **Authors:**

4 Dirksen E. Bussiere*¹, Lili Xie¹, Honnappa Srinivas², Wei Shu¹, Ashley Burke³,
5 Celine Be², Junping Zhao³, Adarsh Godbole³, Dan King³, Rajeshri G. Karki³, Viktor
6 Hornak³, Fangmin Xu³, Jennifer Cobb³, Nathalie Carte², Andreas O. Frank¹,
7 Alexandra Frommlet¹, Patrick Graff², Mark Knapp¹, Aleem Fazal³, Barun Okram⁴,
8 Songchun Jiang⁴, Pierre-Yves Michellys⁴, Rohan Beckwith³, Hans Voshol², Christian
9 Wiesmann², Jonathan Solomon*^{3,5}, Joshiawa Paulk*^{3,5}

10 **Affiliations/Institutions:**

11 ¹Novartis Institutes for Biomedical Research, Emeryville, CA, USA
12 ²Novartis Institutes for Biomedical Research, Basel, Switzerland
13 ³Novartis Institutes for Biomedical Research, Cambridge, MA, USA
14 ⁴Genomics Institute of the Novartis Research Foundation, San Diego, CA, USA

15
16 **⁵Equal contribution statement:**

17 Joshiawa Paulk and Jonathan Solomon jointly supervised this work

18
19 ***Corresponding authors:**

20 ¹Dirksen E. Bussiere (dirksen.bussiere@novartis.com)
21 ³Joshiawa Paulk (josh.paulk@novartis.com)
22 ³Jonathan Solomon (jonathan.solomon@novartis.com)

23
24
25
26
27
28
29
30
31

32 **Abstract**

33 The anti-cancer agent Indisulam inhibits cell proliferation by causing degradation of
34 RBM39, an essential mRNA splicing factor. Indisulam promotes an interaction
35 between RBM39 and the DCAF15 E3 ligase substrate receptor leading to RBM39
36 ubiquitination and proteasome-mediated degradation. To delineate the precise
37 mechanism by which Indisulam mediates DCAF15-RBM39 interaction, we solved the
38 DCAF15-DDB1-DDA1-Indisulam-RBM39(RRM2) complex structure to 2.3 Å. DCAF15
39 has a novel topology which embraces the RBM39(RRM2) domain largely via nonpolar
40 interactions, and Indisulam binds between DCAF15 and RBM39(RRM2) and
41 coordinates additional interactions between the two proteins. Studies with RBM39
42 point mutants and Indisulam analogs validated the structural model and defined the
43 RBM39 alpha-helical degron motif. The degron is found only in RBM23 and RBM39
44 and only these proteins were detectably downregulated in Indisulam-treated HCT116
45 cells. This work further explains how Indisulam induces RBM39 degradation and
46 defines the challenge of harnessing DCAF15 to degrade novel targets.

47

48

49

50

51

52

53

54

55

56

57

58

59

60

61

62

63

64

65

66 **Introduction**

67 Targeted protein degradation (TPD) is an emerging area of small molecule drug
68 discovery¹². In TPD, small molecules do not directly modulate the activity of their target
69 proteins upon binding, but instead bring about the interaction of targets with E3 ligases
70 of the Ubiquitin-Proteasome System (UPS). This compound-induced proximity of the
71 target and E3 ligase leads to removal of the target protein from the cell by proteolytic
72 degradation.

73

74 The Ubiquitin-Proteasome System exists in every cell and functions to regulate most
75 protein half-life³. Conjugation of four or more copies of ubiquitin, a small 76-amino
76 acid protein, allows protein recognition by the 26S proteasome⁴. Upon binding to the
77 proteasome lid, poly-ubiquitinated proteins are pulled into the proteasome tube and
78 cleaved by interior proteolytic active sites into peptide fragments⁵⁶. Ubiquitination is
79 tightly regulated by a three enzyme cascade⁷. Ubiquitin is activated by the E1 enzyme
80 and is transferred to one of the E2 enzymes. The E3 ligases determine which proteins
81 are mono- or poly-ubiquitinated by catalyzing the transfer of ubiquitin from an E2
82 enzyme to a lysine residue on the target protein or ubiquitin. There are over 600 E3
83 ligases encoded in the human genome allowing for the recognition and regulation of
84 large number of diverse substrates, although the structural features recognized
85 (known as the 'degron') are unknown for most of these ligases.⁸

86

87 In TPD, small molecules are used to hijack the E3 ligases of the UPS by a variety of
88 mechanisms. The selective estrogen receptor degraders (SERDs) bind and
89 destabilize the estrogen receptor (ER), increasing its surface hydrophobicity⁹. SERD-
90 bound ER is recognized as unfolded by the protein quality control pathway and is
91 degraded by the UPS¹⁰. Bifunctional degraders are modular molecules that have an
92 E3-binding moiety, a linker, and a target-binding moiety¹¹. Bifunctional degraders
93 literally tether target proteins to E3 ligases to facilitate ubiquitination and degradation.
94 Auxin, a small molecule phytohormone, binds to an E3 ligase forming a new ligase
95 binding surface with increased affinity for the target protein¹². Because auxin was
96 described as a "molecular glue"¹³, this type of TPD molecule, is known as a molecular
97 glue degrader. The IMiD drugs were recently discovered to be molecular glue
98 degraders. They bind the CRBN E3 ligase and create a new binding surface that
99 recruits beta-hairpin containing proteins¹⁴. Another class of TPD molecule is

100 described by the plant hormone Gibberellin (GA). GA binds to its receptor and induces
101 a conformational change that allows receptor binding to its target protein. The
102 receptor-GA-target protein complex is recognized by the E3 ligase leading to target
103 protein degradation¹².

104

105 Indisulam (Fig. 1a), an anti-cancer agent, was recently found to be a TPD molecule.
106 Originally discovered by screening sulfonamides for cancer cell growth inhibition,¹⁵
107 Indisulam stood out by causing G1/S cell cycle arrest and demonstrating efficacy in
108 multiple tumor xenograft models¹⁶. Two seminal papers revealed that Indisulam
109 inhibits cell growth by degrading the essential splicing factor RBM39^{17,18}. Indisulam
110 mediates an interaction between RBM39 and the E3 ligase DCAF15 leading to RBM39
111 poly-ubiquitination and proteasomal degradation. It was unclear whether Indisulam
112 acts allosterically by binding DCAF15 or RBM39 to bring about a conformational
113 change that enhances DCAF15-RBM39 interaction, whether Indisulam stabilizes a
114 weak DCAF15-RBM39 interaction, or whether Indisulam acts as a molecular glue to
115 enhance RBM39 binding to DCAF15 (Fig. 1a).

116

117 In this work, we set out to understand the precise molecular mechanism by which
118 Indisulam brings about the interaction between RBM39 and the DCAF15 E3 ligase
119 substrate receptor. DCAF15-DDB1-DDA1-Indisulam-RBM39 complex structures were
120 determined by both X-ray crystallography and cryogenic electron microscopy (cryo-
121 EM) to 2.3 and 3.5 Å, respectively. The structures reveal that Indisulam is a molecular
122 glue degrader that binds to DCAF15 creating a novel ligase surface that enhances
123 RBM39 binding. This detailed understanding of Indisulam's mechanism of action is
124 the first step towards determining whether the DCAF15 E3 ligase can be
125 reprogrammed by other small molecules to degrade novel targets beyond RBM39.

126

127 **Purification and Characterization of the DCAF15-DDB1-DDA1-Indisulam-RBM39** 128 **complex**

129 The DCAF15-DDB1-DDA1 complex was expressed and purified from SF21 insect
130 cells (Fig. 1b). RBM39(Δ 150) and the second RRM domain of RBM39,
131 RBM39(RRM2), a domain implicated in Indisulam resistance^{17,18}, were expressed
132 and purified from *E. Coli* (Fig.1b; Supplementary Fig. 1). The purified proteins were
133 functionally validated by measuring whether Indisulam-mediated interactions could be

134 detected. In SPR studies, biotinylated DCAF15-DDB1-DDA1 was immobilized on the
135 sensor surface and the response to increasing concentrations of RBM39(Δ 150) or
136 RBM39(RRM2) was measured in the presence of 20 μ M Indisulam (Fig. 1c). Both
137 RBM39(Δ 150) and RBM39(RRM2) bound DCAF15-DDB1-DDA1 in an Indisulam-
138 dependent manner with similar affinities (K_d s of 109 and 135 nM, respectively). This
139 data suggests that RBM39(RRM2) is sufficient to engage the DCAF15 complex in the
140 presence of Indisulam. DCAF15 complex interaction with RBM39 was also
141 interrogated by analytical ultracentrifugation (AUC). An interaction between the
142 DCAF15-DDB1(Δ BPB)-DDA1 complex and RBM39(Δ 150) was detected in the
143 presence of Indisulam, but not with a DMSO vehicle control (Fig. 1d). In the absence
144 of Indisulam, no interaction between the DCAF15 complex and RBM39 could be
145 detected by AUC even upon increasing RBM39(Δ 150) concentrations up to 80 μ M
146 (Supplementary Fig. 2).

147

148 Isothermal calorimetry (ITC) was used to measure binding between Indisulam and the
149 purified proteins in the absence of RBM39 (Fig. 1e). Indisulam binds the DCAF15-
150 DDB1(Δ BPB)-DDA1 complex with a weak affinity of approximately 17 μ M K_d . This
151 weak interaction was confirmed by 1 H saturation transfer difference (STD) NMR,
152 where STD peaks for Indisulam were only detected in the presence of 1 μ M DCAF15-
153 DDB1-DDA1 (Supplementary Fig. 3). No STD peaks were detected between
154 Indisulam and RBM39(Δ 150) alone (indicating a K_d of >50 μ M). Consistent with
155 previous reports, Indisulam binds potently in the presence of both the DCAF15-
156 DDB1(Δ BPB)-DDA1 complex and RBM39(Δ 150) (187 nM K_d), suggesting that
157 Indisulam engages both DCAF15-DDB1-DDA1 and RBM39 to form a quaternary
158 complex^{17,18}.

159

160 **Structure determination of DCAF15-DDB1-DDA1-Indisulam-RBM39 complexes** 161 **by X-ray crystallography and cryo-electron microscopy**

162 The three-dimensional structure of human DCAF15-DDB1(Δ BPB)-DDA1-
163 RBM39(RRM2) in complex with Indisulam was determined by X-ray crystallography
164 (Fig. 2). The human DCAF15-DDB1-DDA1-RBM39(RRM2)-Indisulam co-structure
165 was solved by cryo-electron microscopy (Fig. 2c; Supplementary Fig. 4). The electron
166 density maps for both structures were determined independently, thereby illustrating

167 the structure by two separate methods. To allow determination of the most biologically
168 relevant structure, care was taken to only minimally alter the proteins by mutation or
169 deletion if necessary. The only necessary change was to delete the BPB domain of
170 DDB1 to obtain large, well diffracting crystals for the X-ray studies; the sequence of
171 DCAF15 was not modified. The resolution of the X-ray crystallography and EM
172 structures are 2.3 Å and 3.5 Å, respectively. Crosslinking and mass spectrometer
173 analysis of the DCAF15-DDB1-DDA1 complex provided important spatial constraints
174 for the modeling and is described in Supplementary Fig. 5. Full statistics and methods
175 are provided in Table 1 and the Methods section.

176

177 **The structure and topology of DCAF15**

178 DCAF15 forms direct interactions with DDB1, DDA1, and RBM39(RRM2) in the multi-
179 protein complex (Fig. 2b). Full-length DCAF15 comprises a novel fold of 6 α -helices
180 and 22 largely anti-parallel β -sheets (Fig. 2a)¹⁹. DALI analysis²⁰ suggests some
181 topological similarity with WD repeats from proteins such as WD40 repeat containing
182 protein 5 (PDB accession code 4CY1²¹ and others^{22,23}) and SWD1-like protein (PDB
183 accession code 6E29²⁴), but the root-mean-square-deviation (RMSD) overlap with
184 these proteins is quite high (>4 Å), indicating that there are only disparate regions of
185 structural similarity. Moreover, the DCAF15 fold is topologically less symmetric than
186 these domains which suggests that DCAF15's fold is distinct from typical WD-type
187 domains²⁵. DCAF15 exhibits three disordered regions consistent with PONDR²⁶
188 predictions: residues 1-31 at the N-terminus and residues 272-385 and 398-416 in the
189 middle of the protein. The remainder of DCAF15 is well-ordered, including the C-
190 terminus, which is sequestered within the body of the protein, proximal to the N-
191 terminus.

192

193 Near the N-terminus of DCAF15 is a helix-loop-helix (residues 35-59) which mediates
194 its interaction with DDB1, a feature shared with other CRL4 E3 ligase substrate
195 receptors²⁷⁻²⁹ (Fig. 2d). The helix-loop-helix inserts into the large cleft formed between
196 the BPA and BPC domains of DDB1. It is positioned into the cleft by a salt bridge
197 between Arg60 of DCAF15 and Glu538 of the DDB1-BPC domain and interacts mainly
198 with DDB1 by nonpolar shape complementarity with occasional side-chain mediated
199 hydrogen bonds. The helix-loop-helix also contributes to an unusual feature of

200 unknown significance, an 'arginine ladder', where Arg52 and Arg55 from the DCAF15
201 helix-loop-helix and Arg114 from the DDB1 PBA domain stack against each other and
202 point to the same approximate region in space. The relative orientation of the two
203 helices is ensured by complimentary hydrophobic packing on one side of each helix
204 and the motif is ended by two consecutive prolines, Pro58 and Pro59.

205

206 **DDA1 stabilizes the DCAF15/DDB1 complex**

207 DDA1 is highly-ordered: residues 4-44 form a strand which snakes around the surface
208 of DDB1, residues 45-49 form a β -strand, and residues 53-76 form an α -helix (Fig.
209 3a). Residues 1-3 and 77-102 of DDA1 are disordered, consistent with PONDR²⁶
210 predictions. The N-terminus of DDA1 binds to the DDB1-binding groove identified by
211 Shabek and colleagues (PDB accession code 6DSZ)³⁰. Interactions are mostly
212 hydrophobic in nature, with insertion of aromatic groups into hydrophobic pockets a
213 reoccurring theme (Tyr11, Phe16, and Phe19 on DDA1). The strand then continues
214 along the face of DDB1, engaging hydrophobic pockets and forming main-chain
215 hydrogen-bonding interactions until the start of the α -helix with residue 53. In its path
216 over the surface of DDB1, DDA1 interacts with both the β -sheets and the loops
217 between them. In many locations along this path, the hydrogen-bonding pattern of the
218 main-chain to areas of DDB1 is equivalent to that of a parallel β -sheet.

219

220 Residues 53-76 of DDA1 form an α -helix which serves to help anchor DCAF15 to
221 DDB1 by bridging interactions between the two proteins. The face of the helix facing
222 towards DCAF15 is predominately hydrophobic, with key polar residues forming
223 specific interactions. For example, DDA1(Trp63) forms a structural water-mediated
224 hydrogen-bond with main-chain amide of DCAF15 (Thr463) and DDA1(Lys66) forming
225 a hydrogen-bond with the main-chain carbonyl of DCAF15(Val533). The opposite face
226 is predominately hydrophilic and makes both direct and water-mediated interactions
227 with the BPA domain of DDB1. For example, DDA1(Arg57) forms a salt-bridge with
228 both the main-chain carbonyls of DDB1(Asn156) and DDB1(Lys200), while
229 DDA1(Gln61) forms a hydrogen-bond with the main-chain carbonyl of DDB1(Glu199).
230 Consequently, reconstitution and differential scanning fluorimetry (DSF) reveals
231 greater stability of the DCAF15-DDB1-DDA1 complex compared to DCAF15-DDB1
232 alone (Fig. 3b). Moreover, knockdown of DDA1 in 293T cells impairs Indisulam-

233 mediated degradation of RBM39 and the subsequent reduction in cell viability (Fig.
234 3c,d), confirming a functional role for DDA1 in DCAF15 cellular activity.

235

236 **RBM39-DCAF15 interactions observed in the complex**

237 The RBM39(RRM2) domain has a typical RNA-recognition motif structure comprised
238 of two α -helices positioned against four anti-parallel β -sheets^{31,32}. The RRM2 domain
239 is positioned into a cleft existing between $\alpha 6$ and $\beta 20$ of DCAF15 with the RRM2
240 central α -helix (residues 261-273) positioned proximal to $\beta 9$ and $\alpha 6$ in DCAF15. While
241 the majority of the interactions between RBM39(RRM2) and DCAF15 are nonpolar,
242 the majority of the polar interactions occur between DCAF15 and the central alpha
243 helix of RBM39 (Fig. 4a,b). RBM39(Glu271) positions RBM39(Arg267) via a salt-
244 bridge to coordinate π - π interactions³³ with DCAF15(Phe139) and DCAF15(Phe157)
245 (Fig. 4a); RBM39(Glu271) also forms a direct salt-bridge with DCAF15(Arg178).
246 These interactions are important for Indisulam activity, as the Glu271Gln mutation
247 reduces RBM39 recruitment to DCAF15 by ~1000-fold as measured by fluorescence
248 polarization (Fig. 4c,d). RBM39(Pro272) is positioned within a small hydrophobic
249 pocket on DCAF15 and, like RBM39(Gly268), maintains close surface contact
250 between RBM39 and DCAF15. Disrupting these contacts by Gly268Val or Pro272Lys
251 mutations ablates Indisulam-induced RBM39 binding. A Pro272Ser mutation is better
252 tolerated, but lowers binding affinity by ~6-fold, suggesting the importance of
253 hydrophobic character at this position.

254

255 As nonpolar surface contacts are key contributors to RBM39-DCAF15 interaction, the
256 MOE “patch analyzer” tool³⁴ was used to characterize the RBM39(RRM2)-DCAF15
257 interface. Approximately 5.5% of the DCAF15 surface and 26.3% of the RBM39
258 surface is sequestered from solvent and engaged in protein-protein or protein-
259 compound interactions. The largest hydrophobic patch (140 Å²) on RBM39 is formed
260 by residues in and around the central helix and overlaps partially with a large
261 hydrophobic patch present on DCAF15. In addition, there are four other hydrophobic
262 patches in DCAF15 that are in contact with RBM39 and sequestered from solvent.
263 The total nonpolar area on DCAF15 involved in the interaction with RBM39 is
264 approximately 590 Å², likely comprising the bulk of DCAF15-RBM39 binding energy.

265

266 While non-polar interactions dominate the DCAF15-RBM39 interface, there are also
267 occasional polar interactions at the periphery. For example RBM39(Arg275)
268 hydrogen-bonds with DCAF15(Ser173), albeit with suboptimal geometry, while
269 RBM39(Lys306) forms a weak hydrogen-bond with DCAF15(Thr543) (Fig. 4a).
270 Interestingly, neither of these peripheral interactions appear critical for RBM39
271 recruitment, as substituting alanine for RBM39(Lys306) or RBM39(Arg275) is largely
272 tolerated. Overall, while these DCAF15-RBM39 interactions are incapable of
273 maintaining DCAF15 and RBM39 binding on their own (Fig. 1d), these largely nonpolar
274 contacts are needed for Indisulam-mediated recruitment.

275

276

277 **The structural basis by which Indisulam enhances RBM39 binding to DCAF15**

278 Indisulam binds between the RBM39(RRM2) central helix and β 9, β 16, and α 6 of
279 DCAF15 (Fig 4b). A polar cation- π interaction likely occurs between the heterocycle
280 and DCAF15(Gln232), which is positioned adjacent to the chloro-indole group of
281 Indisulam. The chloro-indole group of Indisulam binds in a hydrophobic pocket
282 comprised of the aliphatic face of Thr230, Phe235 and Val559 from DCAF15, and also
283 RBM39(Met265). RBM39(Gly268) also forms a periphery of the hydrophobic pocket.
284 The phenyl-sulfonamide is positioned between several aliphatic sidechains, including
285 DCAF15(Ala234), DCAF15(Thr262), and RBM39(Met265). Mutations at
286 RBM39(Met265) and RBM39(Gly268) dramatically impact recruitment (Fig. 4d),
287 suggesting that these residues contribute significantly to the DCAF15 binding-pocket.

288

289 The central sulfonamide accepts two hydrogen-bonds from the main chain amides of
290 DCAF15 Ala234 and Phe235; the geometry of these interactions is near-optimal. It
291 should be noted that both MoKa³⁵ calculations and experimental pKa determination
292 show that the nitrogen of the central sulfonamide bears a negative charge
293 (Supplementary Fig. 6). This nitrogen forms water-mediated hydrogen-bonds with
294 both RBM39(Thr262) and RBM39(Asp264). Given that alanine substitution at these
295 positions abrogate binding by ~2 fold, these interactions appear to contribute to
296 RBM39 recruitment albeit modestly. The distal sulfonamide donates a hydrogen-bond
297 from the nitrogen to a structural water which in turn hydrogen-bonds to the main-chain
298 carbonyl of Asn260 of RBM39. The edge of this group exits the body of the complex

299 towards bulk solvent. Altering the flexibility at this position by alanine substitution
300 improves binding by ~3-fold, illustrating its positive contribution.

301

302 From a conceptual view, Indisulam interactions largely complete the full
303 complementarity lacking at the DCAF15-RBM39(RRM2) interface. While several polar
304 interactions are found between Indisulam and RBM39, few appear crucial for
305 recruitment. The most consequential perturbations involve disruption of nonpolar
306 interactions with the indole and terminal phenyl group of Indisulam, as well as those
307 that disrupt nonpolar DCAF15-RBM39 surface contacts.

308

309

310 **Using Indisulam analogs to identify important chemical features driving RBM39** 311 **recruitment to DCAF15**

312 To assess the structural model and to better understand the plasticity of the small
313 molecule binding pocket, Indisulam analogs were tested for their ability to recruit
314 RBM39 to the DCAF15-DDB1-DDA1 complex using a biochemical time-resolved
315 fluorescence resonance energy transfer (TR-FRET) assay (Fig. 5a). The chloro group
316 at position R1 in Indisulam can be substituted by nonpolar groups of similar volume,
317 such as methyl and nitrile (compounds **1-2**; Fig. 5b,c). The nitrile group, a known
318 chlorine isostere, is especially effective and improves the EC₅₀ to 1.21 μM.
319 Substitution of the chloro group with a proton at position R1 (compound **3**) is not
320 tolerated. The proton substitution removes ~38 Å² of hydrophobic surface interaction
321 (~0.95 kcal/mol of binding energy³³) and would likely compromise the positioning of
322 the remainder of the compound-protein contacts.

323

324 The contributions of the terminal sulfonamide at position R3 are explored using
325 compounds **4-7**. Compound **4** replaces the terminal sulfonamide with a dimethyl-
326 sulfonamide at position R3 combined with a methyl replacement at position R1. This
327 weakens the EC₅₀ approximately 4-fold relative to Indisulam, roughly equivalent to the
328 4-fold difference for the methyl substitution alone. This suggests that the dimethyl-
329 sulfonamide substitution is well tolerated. The two methyl groups can make
330 hydrophobic contacts, maintaining non-polar surface area, while the nitrogen
331 maintains hydrogen-bonding to the structural water which bridges its interaction to the
332 backbone carbonyl of Asn260 on RBM39. In compound **5**, the terminal sulfonamide

333 was replaced with a proton, removing the hydrogen bond donor at this position.
334 RBM39 recruitment EC_{50} was reduced 11 fold suggesting a loss of ~1.4 kcal/mol of
335 binding energy which is consistent with the binding energy provided by a hydrogen-
336 bond. In compounds **6** and **7** the terminal sulfonamide was replaced with an amine or
337 methyl amine which are hydrogen bond donors. Additionally, the chloro group at
338 position R1 was replaced with the effective nitrile and a methyl group replaced the
339 hydrogen at position R2. Compounds **6** and **7** maintain strong RBM39 recruitment
340 suggesting that the terminal sulfonamide can be replaced by other hydrogen bond
341 donor groups.

342

343 Compound **7** degrades cellular RBM39 and reduced HCT116 viability with similar
344 potency to Indisulam (Supplementary Fig. 7). STD NMR epitope mapping predicts that
345 the nitrile-methyl-indole ring of compound **7** interacts with DCAF15, whereas the
346 central phenyl group is more exposed to solvent in the absence of RBM39
347 (Supplementary Fig. 8). These data are consistent with the predicted binding pose of
348 Indisulam and suggest that the terminal amine on **7** may represent an 'exit vector' for
349 attachment of large substituents. We have confirmed these findings by solving the
350 DCAF15-DDB1(Δ BPB)-DDA1-RBM39(RRM2) X-ray crystal structure in complex with
351 **7** (data not shown), which shows that its binding pose is equivalent to Indisulam's.

352

353 Lastly, Compound **8** probes the importance of the central sulfonamide in the
354 recruitment of RBM39. Replacement of the central sulfonamide with an amide ablates
355 RBM39 recruitment. This modification disrupts hydrogen-bonding with the backbone
356 amides on DCAF15, and the amide linker also significantly alters conformational
357 preferences of compound **8**, thereby disrupting its binding. Overall, the observed
358 compound SAR supports the predicted binding mode for Indisulam and highlights
359 regions amenable to further modification.

360

361 **Indisulam selectivity predictions based on critical RBM39 residues**

362 A question of great interest is whether new, yet unidentified proteins can be recruited
363 to DCAF15 by Indisulam. The structure of the complex, RBM39 mutagenesis studies
364 and previously published work^{17,18} suggest that RBM39 residues Met265, Gly268,
365 Glu271, and Pro272 in the central alpha helix are necessary for Indisulam-mediated

366 DCAF15 binding. An alpha helical “X¹XXM⁴XXG⁷XXEP¹¹” sequence was defined as a
367 putative degron motif.

368

369 The bioinformatics workflow is summarized in Figure 6a. To identify compatible
370 proteins with the putative degron motif, 20,421 unique human protein sequences from
371 uniprot were accessed (<http://www.uniprot.org>). 6,475 of these entries had associated
372 x-ray/NMR structures. For proteins with known structures, 3,425 proteins were
373 identified with a glycine at position 7 of the alpha helix, and a helix RMSD of less than
374 2Å. The helix RMSD is determined by first aligning all identified helices containing
375 glycine at the correct position to the RBM39(Thr262-Pro272) central helix from the
376 DCAF15 co-structure, and then calculating a backbone RMSD of the two helices using
377 the alpha-carbons. Next, steric clashes of these target proteins with DCAF15 were
378 calculated, where clashes of less than 10 heavy atoms between DCAF15 and the
379 target protein were considered acceptable. This yielded 1787 targets with good helix
380 overlay and minimal steric clash. While these protein entries may be sterically
381 compatible with Indisulam-bound DCAF15, only the helices from RBM39 and RBM23
382 comprised sequences matching our putative degron motif. Expression proteomics
383 studies in HCT116 cells treated with 10 µM indisulam for 4 hours showed that RBM39
384 and RBM23 were the most significantly downregulated proteins (>2 fold over DMSO,
385 Fig. 6b). While ZNF277 was also identified as a potential target from these studies,
386 Western blot analysis confirmed that only RBM23 and RBM39 were reduced by
387 indisulam (Fig. 6c).

388

389 **Discussion**

390 TPD is a promising new area of drug discovery focused on developing small molecules
391 that bring “difficult-to-drug” targets in close proximity to E3 ligases to induce UPS-
392 dependent target degradation¹². Understanding the mechanism of action of the few
393 known TPD molecules will drive progress in this young field. Our work leveraged
394 structural biology, biophysics, and chemical and genetic variomics to study the TPD
395 molecule Indisulam and to understand precisely how Indisulam recruits RBM39 to the
396 DCAF15 E3 ligase substrate receptor.

397

398 The co-structure reveals that Indisulam behaves as a molecular glue degrader rather
399 than an allosteric inducer of dimerization like Gibberellin¹². DCAF15, with its novel

400 fold, embraces RBM39(RRM2) with Indisulam interacting with both proteins to
401 promote a suitable interface (Fig. 2b). Indisulam sits in a well-defined pocket formed
402 by DCAF15 and coordinates several direct and water-mediated interactions with both
403 RBM39 and DCAF15 (Fig. 4b). There is also a series of interactions between DCAF15
404 and RBM39. These DCAF15-RBM39 interactions are insufficient to enable binding on
405 their own, as interaction in the absence of Indisulam could not be detected by AUC
406 (Supplementary Fig. 2) or SPR (data not shown). It is therefore unlikely that Indisulam
407 binds to a site pre-formed by RBM39 and DCAF15 association or stabilizes a basal
408 interaction, ruling out a brefeldin A-like mechanism³⁶. Given that Indisulam fails to
409 bind RBM39 alone (Fig. 1e), it is not a direct destabilizer of RBM39, like the SERDs¹⁰.
410 Indisulam does bind the DCAF15-DDB1-DDA1 complex alone with weak affinity (~17
411 μ M, Fig. 1e) and binds more potently in the presence of RBM39 (187 nM, Fig. 1e).
412 This ~100-fold binding affinity enhancement likely stems from the additional direct and
413 water-mediated polar contacts made between RBM39 and Indisulam, along with the
414 series of nonpolar interactions emerging from the apparent structural complementarity
415 between DCAF15 and RBM39. Overall, the data suggests that an Indisulam-DCAF15
416 interaction precedes association with RBM39, whose recruitment in turn stabilizes
417 Indisulam binding.

418

419 This report provides the first high-resolution structural view of the DCAF15 E3 ligase,
420 a DDB1-CUL4 associated substrate receptor about which little is known. Apart from
421 the reported association with its partners DDA1, DDB1, and associated CRL4
422 components^{17,18}, no additional endogenous binding partners nor substrates have been
423 identified to date. Human papillomavirus (HPV) E6 and E7 proteins, known oncogenic
424 factors capable of recruiting host E3 ligases for the degradation of tumor
425 suppressors^{37,38}, were found to bind DCAF15, however, the biological consequences
426 of this event are unclear³⁹. Given that DCAF15 exhibits significant disorder in our co-
427 structure and comprises a novel fold distinct from the WD40-type domain seen among
428 other CRL4 E3 substrate receptors (e.g. CRBN, DDB2), additional binding partners
429 unique to DCAF15 are likely to be implicated in its biology and may help to facilitate
430 the identification of novel substrates. Like other DDB1-associated E3 ligases, a helix-
431 loop-helix mediates interaction between DCAF15 and DDB1 along with several
432 hydrogen-bonding, water-mediated, and nonpolar interactions (Fig. 2d).

433

434 DDA1, a member of the E2-interacting DDD complex⁴⁰ with de-etiolated 1 (DET1)
435 and DDB1, was pulled down with DCAF15 in the presence of Indisulam^{17,18}. While
436 immunoprecipitation (IP) studies have found DDA1 to be associated with several
437 CRL4-DCAFs with the exception of DDB2⁴¹, its impact on CRL4 biology is largely
438 unknown. A recent report suggests that DDA1 regulates lenalidomide-mediated
439 ubiquitination of IKZF1/3 through its association with CRBN-DDB1⁴², although CRBN
440 IP studies fail to capture DDA1 as a binding partner^{43,44}. DDA1 improves the thermal
441 stability of the DCAF15-DDB1 complex and is required for Indisulam-mediated
442 degradation of RBM39 (Fig. 3), suggesting a significant role for DDA1 in DCAF15-
443 CRL4 complexes. The N-terminus of DDA1 binds to a previously reported DDB1-
444 binding groove³⁰, while the C-terminus forms an α -helix which serves as an interface
445 to help anchor DCAF15 to DDB1 through bridging interactions. Crosslinking mass
446 spectrometry studies (Supplemental Fig. 6) suggest DDA1 displays dynamic mobility,
447 signifying possible roles in substrate recognition or ubiquitination. Further work will be
448 required to elucidate the potential roles of DDA1 in CRL4 ubiquitination.

449

450 A key question for drug discovery and design is whether Indisulam and related aryl
451 sulfonamides analogs could potentially provide a route to novel DCAF15-based
452 molecular glue degraders, parallel to the development of IMiD analogs capable of
453 degrading a diversity of targets through CRBN¹⁴. From a compound perspective,
454 IMiDs bind CRBN with high affinity (100-200 nM)^{14,29} whereas Indisulam binds
455 DCAF15 weakly (~17 μ M). For Indisulam, RBM39 target binding is needed to potently
456 engage the DCAF15 E3 ligase. Regions of Indisulam required for DCAF15 binding
457 overlap with regions needed for target recruitment (Fig. 4b), unlike IMiDs where there
458 is a separation between the CRBN binding region, the glutaramide warhead, and the
459 recruitment region. IMiD-CRBN complexes appear uniquely poised to recruit proteins
460 bearing a beta hairpin structural motif^{14,45}. This is achieved primarily through IMiD-
461 bound CRBN interactions with a precise spatial arrangement of backbone on the beta
462 hairpin degron^{29,45-47}. Selectivity for a given beta hairpin protein can be achieved
463 through compound-mediated interactions with unique side-chain features on the
464 recruited target^{14,29,46,47}. DCAF15-bound Indisulam primarily engages with side-chains
465 of the RBM39 target and coordinates only a few interactions with backbone elements
466 (Fig. 4b), likely underpinning its remarkable selectivity. Proteomics analysis of

467 HCT116 cells treated with 10 μ M Indisulam for 4 hours only showed downregulation
468 of RBM39 and RBM23 (Fig. 6b,c), two RRM domain-containing protein sharing nearly
469 89% identity within these RRM domains. As our bioinformatics analysis reveals, only
470 these two proteins harbor the requisite glycine-containing alpha helix with critical
471 residues able to mediate interactions with both Indisulam and DCAF15 (Fig. 6a).
472 Moreover, RBM23 harbors this sequence within an RRM domain, likely enabling
473 further nonpolar interactions via complementarity with DCAF15. While other RRM-
474 domain proteins may complement the DCAF15 binding pocket, none bear the critical
475 motif necessary to engage Indisulam to a degree similar to RBM23 or RBM39. We
476 propose that novel DCAF15-binding chemotypes would be required to engage
477 DCAF15 and recruit additional partners in a programmable manner similar to IMiD
478 analogs. DCAF15 binders that separate ligase binding and target recruitment and
479 which coordinate backbone features of a recruited degron could potentially provide a
480 route to programmable DCAF15 degraders. However, such compounds and structural
481 degrons have yet to be identified and this represents the challenge for the
482 development of future DCAF15 molecular glues degraders.

483

484 **Methods**

485 *Cloning, protein expression and purification*

486 The gene for DCAF15 was codon-optimized and cloned into a pFastBac vector with
487 an N-terminal His-ZZ-3C tag. DDB1, DDB1- Δ BPB (DDB1 with a residue 398-701
488 deletion), and DDA1 were each cloned into a pFastBac vector without an associated
489 tag. The pFastBac constructs were used to generate baculovirus using the Bac-to-
490 Bac method (Bac-to-Bac[®] Baculovirus Expression System, ThermoFisher). The
491 baculovirus was amplified in SF21 cells (ThermoFisher). DCAF15 was co-expressed
492 with DDB1 (or DDB1- Δ BPB) and DDA1 in SF21 cells seeded at a density of 1.5×10^6
493 cells/mL and synchronously infected with the recombinant baculoviruses at a volume
494 of 2%:4%:4%. The cultures were grown in 2-L glass Erlenmeyer flasks in serum-free
495 media with agitation at 120 rpm for 48 hours at 27 °C. Cells were harvested two days
496 post-infection, flash frozen, and stored at -80 °C.

497 Cell pellets were resuspended in lysis buffer consisting of 50mM HEPES, pH 7.5, 500
498 mM NaCl, 20mM imidazole, 10% Glycerol (v:v), 2mM TCEP, universal nuclease
499 (Pierce), and 3x protease inhibitor (Roche) and lysed using a Dounce homogenizer.

500 The clarified cell lysate was mixed with 10 mL Ni-NTA resin and incubated at 4 °C for
501 4 hours. The resin was washed with IMAC buffer A, which consisted of 50mM HEPES,
502 pH7.5, 500 mM NaCl, 20mM Imidazole, 10% glycerol (v:v), and 2mM TCEP. The
503 protein was eluted with IMAC buffer B, which consisted of 50mM HEPES, pH7.5, 500
504 mM NaCl, 500mM imidazole, 10% glycerol (v:v), and 2mM TCEP. The fractions
505 containing the His-ZZ-3C-DCAF15-DDB1-DDA1 complex were combined and treated
506 with 3C protease overnight in dialysis buffer consisting of 50mM HEPES, pH7.5, 400
507 mM NaCl, and 1mM TCEP. The cleaved protein was then purified by a 5 ml HisTrap
508 HP column on an AKTA Avant system (GE Healthcare). The flow through was
509 combined and diluted with buffer C, which consisted of 50mM HEPES pH7.5, and
510 2mM TCEP, and purified by a 5 mL HiTrap Q HP column. The protein was eluted with
511 a 100 mL linear gradient of 200 mM to 500 mM NaCl in buffer C. Fractions containing
512 the complex were concentrated and further purified by a Superdex 200 26/60 column
513 (GE Healthcare) in buffer D, which consisted of 50mM HEPES, pH7.5, 300 mM NaCl,
514 and 1mM TCEP. The yield of purified complex following this procedure was
515 approximately 15 mg of DCAF15-DDB1-DDA1 per liter of culture. The molecular
516 weights of the proteins in the complex were confirmed by LC/MS. The intact protein
517 mass was detected by LC/MS on an Open Access MS system (Agilent 1290 UHPLC
518 + Agilent 6530 QToF) and analyzed by the MassHunter software.

519 RBM39 (residues 151-end) and RBM39 (residues 250-328) were each cloned into
520 pET30b vector with an N-terminal His-ZZ-3C tag. Q5 mutagenesis (NEB) was
521 performed on these constructs to generate reported mutants using manufacturer's
522 protocol. Proteins were expressed in *E. coli* BL21(DE3) cells (16 °C for 18 hrs followed
523 by induction by 1 mM IPTG). Cell pellets were resuspended in lysis buffer containing
524 50mM HEPES, pH 7.5, 500 mM NaCl, 20mM imidazole, 10% Glycerol (v:v), 2mM
525 TCEP, and 1x HALT protease inhibitor cocktail (ThermoFisher). After lysis by
526 sonication, the protein was purified by a HisTrap column, cleaved by 3C protease, and
527 purified again by a HisTrap column. The cleaved protein was further purified by a
528 Superdex 200 16/60 column (GE Healthcare) in 50mM HEPES, pH7.5, 300 mM NaCl,
529 and 1mM TCEP. For His-ZZ-RBM39(151-end) variants, proteins were purified by
530 batch Ni-NTA bead purification (1 mL slurry/1L culture; Qiagen) and further purified by
531 a Superdex 200 16/60 column (GE Healthcare) in 50mM HEPES, pH7.5, 300 mM
532 NaCl, and 1mM TCEP.

533 *Surface plasmon resonance binding analysis*

534 500 resonance units (RU) of Biotinylated DCAF15-DDB1-DDA1 was immobilized to a
535 streptavidin SA Sensor Chip (GE Healthcare Life Sciences) in a running buffer
536 consisting of 50 mM HEPES, pH 7.5, 300 mM NaCl, 1 mM TCEP, 0.05% (v:v) Tween-
537 20 supplemented with 20 μ M Indisulam. All SPR studies were performed on a
538 Biacore T200 instrument (GE Healthcare Life Sciences). Following capture, any
539 remaining streptavidin sites on both the reference and active channels were blocked
540 with biocytin. The association and dissociation steps of a dilution series of RBM39
541 (Δ 150) or RBM39(RRM2) domains were performed in running buffer in the presence
542 of excess Indisulam. All sensorgrams shown are reference subtracted with solvent
543 correction procedures implemented. Data were fit to both steady state and a 1:1 kinetic
544 model using Biacore evaluation software and gave equivalent dissociation constants
545 (K_d).

546

547 *Analytical ultracentrifugation*

548 Experiments were performed in a Beckman Optima analytical ultracentrifuge equipped
549 with double sector, charcoal-filled centerpieces (12 mm path length, sapphire
550 windows). In brief, 2.5 μ M DCAF15-DDB1(Δ BPB)-DDA1 and 10 μ M of His-ZZ-
551 RBM39(Δ 150) were incubated with and without 12.5 μ M Indisulam for 60 min in 50
552 mM HEPES, pH 7.5, 300 mM NaCl, and 1 mM TCEP and subjected to sedimentation
553 velocity at 42,000 rpm for 5 h at 20 °C. For analysis, buffer density, viscosity, and
554 partial specific volumes (derived from amino acid composition) were calculated using
555 SEDNTERP⁴⁸. Rayleigh interferometric fringe displacement sedimentation data was
556 collected and modeled with diffusion-deconvoluted sedimentation coefficient
557 distributions $c(s)$ in SEDFIT⁴⁹.

558

559 *Isothermal calorimetry*

560 Isothermal calorimetry was used to measure the heat of enthalpy of the DCAF15-
561 DDB1-DDA1-RBM39(Δ 150)-Indisulam complex formation using a GE Healthcare
562 autoITC200 at 25 °C. Protein solution in the calorimetric cell containing both DCAF15-
563 DDB1(Δ BPB)-DDA1 complex at 10 μ M and RBM39(Δ 150) at 10 μ M were titrated with

564 Indisulam at 100 μ M, in carefully matched buffers. 19 injections were carried out until
565 the proteins were fully saturated. The control experiments were also carried out
566 accordingly. The resulting binding isotherms were analysed by nonlinear least-
567 squares fitting of the experimental data to models corresponding to a single binding
568 site. Analysis of the data was performed using the MicroCal Origin 7.0 software.

569

570 *NMR Spectroscopy*

571 All NMR experiments were performed on a 600 MHz Bruker Avance III NMR
572 spectrometer equipped with a 5 mm QCI-F cryogenic probe. NMR samples for all
573 saturation transfer difference (STD)⁵⁰ experiments were prepared in 3 mm tubes filled
574 with 170 μ L of 99.9% D₂O buffer containing 50 mM sodium phosphate, pH 7.4, 200
575 mM NaCl, 2 mM deuterated dithiothreitol (DTT), 22.2 μ M 4,4-dimethyl-4-silapentane-
576 1-sulfonic acid (DSS) and 200 μ M of compound. Spectra were recorded in the
577 presence and in the absence of 1 μ M DCAF15/DDB1/DDA1 at 280 K (STD epitope
578 mapping) and 286 K (STD Indisulam binding study). Spectra in the absence of protein
579 were used to confirm that potential compound aggregation does not lead to false-
580 positive STD results.

581

582 The standard Bruker pulse sequence *stdiffesgp* was used for all STD experiments.
583 The on- and off-resonance irradiation frequencies were set to 0.33 ppm and -33 ppm,
584 respectively. Selective saturation of the protein was achieved by a train of Sinc-shaped
585 pulses of 50 ms length each. The total duration of the saturation periods were varied
586 from 100 ms to 10 s (4 s for the Indisulam study). The recycling delay was set to 10 s
587 in all experiments. The total number of scans (dummy scans) was 48 (16), a spectral
588 width of 16 ppm was used and the number of points recorded was 32k.

589

590 ¹H-STD NMR spectra were multiplied by an exponential line-broadening function of 3
591 Hz prior to Fourier transformation. The on-resonance spectra were subtracted from
592 the off-resonance spectra to obtain difference spectra, which were used for analysis.

593

594 The compound ¹H-NMR signals were assigned by using standard small molecule
595 NMR structure elucidation experiments (¹H-1D, ¹³C-1D, ¹H,¹H-COSY, ¹H,¹³C-HSQC,

596 ^1H , ^{13}C -HMBC). The analysis leading to the epitope map was performed using the
597 equations described in Chatterjee et al.^{50,51}.

598

599 *Crosslinking, MALDI-MS and proteolytic digestion*

600 The purified DDB1-DDA1-DCAF15 complex was incubated at a final concentration of
601 0.1 μM in 100 μL of 20 mM HEPES, pH 7.5, and 30 mM NaCl with two equivalents of
602 RBM39(Δ 150) and five equivalents of Indisulam for 2 hours at room temperature.

603 The crosslinking reaction was carried out with 600 equivalents of disuccinimidyl
604 sulfoxide (DSSO, Thermo Scientific) for 1.5 hours at room temperature. This is
605 equivalent to a lysine:DSSO molar ratio of 1:6 since DDB1-DDA1-DCAF15-
606 RBM39(Δ 150) contains 103 lysines. The covalent complex formation was analyzed
607 by MALDI-MS prior to quenching the crosslinking reaction with NH_4HCO_3 to a final
608 concentration of 20 mM (Ultraflextreme II, Bruker). The dried droplet method was used
609 with a saturated sinapinic acid solution in $\text{CH}_3\text{CN}/\text{H}_2\text{O}$ at a ratio of (75:25; v:v) with
610 0.1% TFA (v:v). MALDI-MS analyses were performed in linear mode using an external
611 calibration with the protein calibration standard II (Bruker).

612 The crosslinked complex was subsequently denatured with a solution of 3M urea and
613 180 mM NH_4HCO_3 , and then reduced with 12 mM DTT for 1 hour at 56°C. The
614 reduced complex was then alkylated with 36 mM iodoacetamide for 30 minutes at
615 room temperature, and the alkylation reaction was quenched with additional 12 mM
616 DTT. The cross-linked complex solution was diluted 3.5-fold in water and digested with
617 trypsin (sequencing grade modified, Promega) at a 1:5 enzyme to substrate ratio (w:w)
618 at 37°C overnight. The digestion was stopped by adding TFA at 0.1% (v:v) final
619 concentration. The cross-linked peptides were desalted using a Sep-Pak C18 column
620 (Waters), dried under nitrogen at 50°C, and reconstituted in $\text{H}_2\text{O}/\text{CH}_3\text{CN}/\text{HCOOH}$
621 (96:2:2; v:v:v) for the subsequent LC-MSⁿ analyses.

622

623 *LC-MSⁿ analysis*

624 LC-MSⁿ data were acquired on a Lumos, Orbitrap mass spectrometer equipped with
625 an ultra-HPLC Proxeon Easy-nLC 1200 (Thermo Scientific). Reverse phase
626 chromatography was performed with an analytical Easy-Spray column (75 μm inner

627 diameter, 250mm length; Thermo Scientific). Cross-linked peptides were separated
628 with a 180 min gradient from 2% to 80 % of CH₃CN in H₂O plus 0.1% HCOOH at a
629 flow rate of 300nL/min. MS data were acquired with a specific DSSO-cross-linked
630 peptide method. Briefly, MS1 was performed in the orbitrap and scanned from 300 to
631 1500 *m/z* with a resolution of 120,000. Only ions with charge state from 4+ to 8+ were
632 selected for MS² scans. The MS² scan in the orbitrap was set to 30,000 with a
633 precursor isolation window at 2 *m/z*. The MS² normalized collision energy was fixed
634 at 25%. MS³ HCD were triggered if a mass difference of 31.972 Da was observed
635 between 2 fragment ions detected on MS2 spectrum (specific to sulfoxide MS
636 cleavable cross-linked peptide). The two most intense ion pair ions were selected for
637 fragmentation with a collision energy set to 30%.

638

639 *MSⁿ Data analysis and crosslink Identification*

640 Data files were analyzed by Proteome Discoverer 2.2 (Thermo Scientific) using the
641 XlinkX node to identify cross-linked peptides and the SEQUEST search engine for
642 unmodified and dead-end-modified peptides. In Proteome Discoverer 2.2, the
643 precursor mass tolerance was set to 10 ppm, the MS² filter for peptide tolerance at 20
644 ppm, and the MS³ peptide fragment tolerance at 0.6 Da. Data was searched with a
645 1% FDR criteria against a restricted database containing the 4 proteins (DCAF15,
646 DDB1, DDA1, and RBM39). Crosslinked peptides identified with Proteome Discoverer
647 were filtered for a confident identification with Xlink score greater than 50. The protein-
648 protein interaction mapping for the complex was visualized with XiNET Viewer⁵².

649

650 *Crystallization and structure solution of the DCAF15-DDB1(Δ BPB)-DDA1- 651 RBM39(RRM2)-Indisulam complex*

652 Initial crystallization screens comprised of 1800 different crystallization conditions
653 utilizing DCAF15-DDB1-DDA1-RBM39(RRM2)-ligand complexes identified crystals
654 with excellent hexagonal morphology. However, these hexagonal crystals were
655 extremely soft and exhibited poor diffraction (approximately 6-8 Å) and extreme
656 radiation sensitivity. These crystals could not be optimized to yield higher resolution
657 diffraction. Initial molecular replacement solutions using a DDB1 search model (PDB

658 accession code 3E0C) and the observation of radiation sensitivity strongly suggested
659 that the crystals had a high solvent content due to the packing arrangement enforced
660 by full-length DDB1 and that the B-propeller domain (BPB) was positioned at a
661 different angle in the complex versus the apo-structure. Also, the initial EM maps
662 showed that the B-propeller domain showed increased flexibility versus the structure
663 of apo-DDB1. Given these observations, a construct in which the BPB domain was
664 deleted was utilized to yield an approximately spherical complex with more possible
665 packing arrangements, as well as reduced flexibility. This protein engineering yielded
666 a well-behaved protein complex that forms crystals with improved robustness and
667 diffraction; these crystals typically diffract to 2.3-2.8 Å.

668 DCAF15-DDB1(Δ BPB)-DDA1-RBM39(RRM2)-ligand complexes were crystallized as
669 follows. DCAF15-DDB1(Δ BPB)-DDA1 at a concentration of 10.0 mg/ml was combined
670 with 1.8 molar equivalents of both RBM39(RRM2) and ligand, respectively. This
671 mixture was incubated on ice for 30 minutes to allow the complex to form and was
672 then spun in an ultracentrifuge at 14,000 rpm for 10 minutes to remove debris and
673 aggregates. Crystallization trays were set up using the hanging drop method in
674 INTELLI-plates using 0.2 ul of protein solution and 0.2 ul of precipitant. A precipitant
675 grid screen consisting of 2% (v:v) TacsimateTM, pH 5.0, 0.1 M sodium citrate tribasic
676 dihydrate, pH 5.6, and 10-20% (w:v) polyethylene glycol 3350, was used. Crystals
677 grew at 18°C in 5 days. Crystals were cryo-protected using well solution
678 supplemented with 25% v:v of glycerol. All data was collected at the Advanced Light
679 Source on beamline 5.0.2 using standard collection protocols at a wavelength of 1 Å,
680 which provided the highest flux. Several distinct and disparate areas of single crystals
681 were used for data collection, and these arcs were combined to yield data sets of high
682 multiplicity.

683 The DCAF15-DDB1(Δ BPB)-DDA1-RBM39(RRM2)-Indisulam co-structure was solved
684 using a hybrid molecular replacement/pseudo-atom approach. An initial molecular
685 replacement solution was executed using an appropriately-pruned search model
686 consisting of the crystal structure of apo-DDB1 (PDB accession code 3E0C) and the
687 NMR structure of RBM39 RRM2 (PDB accession code 2JRS), in the given order. This
688 molecular replacement solution was carefully refined against the X-ray data using a
689 resolution cut-off of all data with an I/σ greater than or equal to 1, corresponding to a

690 resolution cut-off of 2.50 Å, using cross-validation via R_{free} to monitor the suitability of
691 the refinement. Initial electron density maps showed new features and improved
692 information content for both DDB1 and RBM39 (such as different sidechain positions)
693 which were not present in the refined search models. These structures were refined
694 to convergence. At this point, 32% of the mass of the complex was present in the
695 model and the electron density maps showed some features which indicated that
696 DCAF15 was bound. It was possible to visualize the docking helix density and there
697 was noisy density was present for a few β -strands, but these could not be accurately
698 placed, nor could the maps be improved with other standard methods alone, such as
699 solvent-flattening. To prevent having to produce selenomethione-labeled protein, a
700 pseudo-atom approach was used to provide additional phase information. Using the
701 Phenix suite⁵³, the current electron density maps were computationally interrogated in
702 the presence of the already refined DDB1- Δ BPB and RBM39-RRM2 structures and at
703 each position where the electron density map showed a peak at 1σ in the 2Fo-Fc map
704 and at 2σ in the Fo-Fc map, a water molecule was placed. The role of these water
705 molecules was to provide a scattering surrogate for other atoms in both main-chain
706 and side-chains. To allow these pseudo-atoms to more effectively mimic atomic
707 centers, the effective VDW radii was decreased and the real-space correlation cutoff
708 used in the atom placement was effectively disabled. This DDB1- Δ BPB:RBM39-
709 RRM2:pseudo-atom model was carefully refined to prevent over-fitting (again via
710 observation of R_{free}), followed by additional placement of pseudo-atoms and
711 refinement of the model until convergence had been reached. To minimize bias, the
712 electron-density maps from this step were subjected to both solvent-flattening and
713 histogram matching, and the positions of all pseudo-atoms were visually inspected
714 against these electron density maps and appropriately repositioned and/or deleted.
715 This adjusted model, which consisted of a DDB1- Δ BPB:RBM39-RRM2:pseudo-atom
716 'complex', had an R/R_{free} of approximately 28%/35% and showed numerous additional
717 features, including the majority of the β -strands which comprise the body of DCAF15,
718 as well as the chain of DDA1. The electron-density map from this model was again
719 subjected to solvent-flattening and histogram matching and used by SOLVE to
720 computationally build a skeleton for the protein as well as assignment of amino acid
721 sequence where possible. These maps also unambiguously identified the binding site
722 of Indisulam as well as all bordering amino acids, which were fit. The skeleton

723 coordinates, as well as order/disorder and secondary structure predictions were then
724 used to build the remainder of both DCAF15 and DDA1 using standard 2Fo-Fc and
725 Fo-Fc maps, as well as 'feature-enhanced' maps. The structure of the complex was
726 consistent with the cross-linking data and EM maps. The structure of the complex
727 was then refined to convergence via multiple cycles of manual rebuilding and
728 refinement using data from 69.10 -2.3 Angstroms (consistent with a CC1/2 cutoff of
729 0.493 for the high-resolution data) using both the Phenix⁵³ and BUSTER⁵⁴ program
730 suites. The final structure of the complex had an R of 20.4% and an R_{free} of 24.9%.
731 The final crystal co-structure consists of 1,392 residues, Indisulam, a glycerol
732 molecule, and 875 waters. The co-structure has a clashscore of 10.65. The model
733 has 93.78% of the protein residues in the favored region of the Ramachandran plot,
734 6.00% in the allowed region, and 0.22% as outliers. The Molprobity score is 2.28⁵⁵;
735 there are extremely regions at the periphery of DCAF15 where it is difficult to fit
736 appropriate rotamers.

737 Please note that to execute such a phasing strategy, it is necessary to have complete,
738 well-measured data, particularly for a complex of this size. The DCAF15-
739 DDB1(Δ BPB)-DDA1-RBM39(RRM2)-Indisulam co-structure was subsequently used
740 to solve the DCAF15-DDB1(Δ BPB)-DDA1-RBM39(RRM2) co-structure with
741 compound **7** by molecular replacement.

742

743 *Cryo-EM sample preparation and data acquisition*

744 Two μ M of the DCAF15-DDB1-DDA1 complex was incubated with 200 μ M of
745 Indisulam and 10 μ M of RBM39(RRM2) at 4°C for 30 minutes. 4 μ L aliquots of the
746 complex were applied to glow-discharged, 300-mesh Quantifoil R 1.2/1.3 grids
747 (Quantifoil, Micro Tools GmbH). These grids were blotted for 3 seconds and
748 subsequently plunged into liquid ethane using an FEI Mark IV Vitrobot operated at 4°C
749 and 90% humidity. High-resolution images were collected with a Cs-corrected FEI
750 Titan Krios TEM operated at 300 kV equipped with a Quantum-LS Gatan Image Filter
751 and recorded on a K2-Summit direct electron detector (Gatan GmbH). Images were
752 acquired automatically (with EPU, ThermoFisher) in an electron-counting mode, using
753 a calibrated magnification of 58140 corresponding to a magnified pixel size of 0.86 Å.

754 Exposures of 12 seconds were dose-fractionated into 40 frames. The total exposure
755 dose was $\sim 50 \text{ e}^- / \text{\AA}^2$. Defocus values per frame varied from -0.8 to -2.4 μm .

756

757 *Image processing of cryo-EM data*

758 The collected frames were processed using cisTEM⁵⁶. Whole-frame motions were
759 corrected, followed by estimation of the contrast transfer function (CTF) parameters.
760 Images with CTF fits to 4 \AA or better were selected. 450,000 coordinates were then
761 automatically selected based on an empirical evaluation of maximum particle radius
762 (70 \AA), characteristic particle radius (50 \AA), and threshold peak height (4 standard
763 deviations above noise). Three rounds of 2D classification into 50 classes were
764 performed to remove false positives and suboptimal particles. The remaining 150,371
765 particles were used for ab initio 3D reconstruction with applied C1 symmetry. These
766 particles were subsequently used for iterative 3D classification and auto refinement,
767 which resulted in an approximately 3.3 \AA resolution map. Maps were auto-sharpened
768 by using the Phenix suite⁵³. The resolution values reported are based on the gold-
769 standard Fourier shell correlation curve (FSC) criterion of resolution cutoff of 0.143.
770 Simultaneously, a total of 415203 particles were extracted for processing using the
771 Relion 3 software package⁵⁷. Particle sorting included two cycles of reference-free 2D
772 classification. The 386408 particles in the best 2D classes were used for 3D
773 refinement. The generation of initial model was carried out in cisTEM⁵⁶. 3D
774 classification was performed without alignment to separate different conformational
775 states (Relion3). Auto-refinement of particles with a soft mask (relion_create_mask)
776 around complex resulted in a 3.54 \AA resolution map. The crystal structure of DDB1
777 (PDB accession code 5JK7) was manually fitted into the cryo-EM map using Coot⁵⁸.
778 The DDA1 density was located using in-house cross-linking data and DDA1 model
779 was built with a partially assigned sequence. The NMR structure of the RBM39 RRM2
780 domain (PDB accession code 2JRS) was manually fitted to the cryo-EM map.
781 Indisulam density could be located at the interface of DCAF15 and RBM39 domain.
782 To complete the model of DCAF15, initially secondary structures were placed into the
783 EM maps using poly-alanine α -helices and β -sheets. Sequence assignments of the
784 observed secondary structure were then completed using the crystal structure of the
785 DCAF15 complex and side-chains were added as appropriate. This atomic model was

786 subjected to multiple cycles of model rebuilding using Coot and real space refinement
 787 against the map using Phenix⁵³. This process resulted in an atomic model of the
 788 ternary complex that fits well into the cryo-EM density map. The final EM co-structure
 789 consists of 1,308 residues and Indisulam. The co-structure has a clashscore of 9.00⁵⁵.
 790 The model has 88.77% of the protein residues in the favored region of the
 791 Ramachandran plot, 10.21% in the allowed region, and 1.03% as outliers.

792 **Table 1. X-ray crystallographic data collection and refinement statistics (molecular replacement**
 793 **with iterative pseudo-atom phasing)**

	DCAF15-DDB1(Δ B-PBP)- DDA1-RBM39(RRM2)- Indisulam
Data collection	
Space group	P2 ₁ 2 ₁ 2 ₁
Cell dimensions	
<i>a</i> , <i>b</i> , <i>c</i> (Å)	81.032, 93.778, 264.639
α , β , γ (°)	90.00, 90.00, 90.00
Resolution (Å)	88.39 - 2.30 (2.34-2.30)
<i>R</i> _{merge}	0.248 (3.598)
<i>R</i> _{pim}	0.075 (1.119)
<i>CC1/2</i>	0.993 (0.483)
<i>I</i> / σ <i>I</i>	6.1 (0.6)
Wilson B-factor	54.226
Completeness (%)	99.8 (98.7)
Total observations	1,072,704 (51,704)
Unique observations	90,574 (4,436)
Redundancy	11.8 (11.7)
Refinement	
Resolution (Å)	69.10-2.30 (2.31-2.30)
Number of reflections	90,501 (1,811)
<i>R</i> _{work} / <i>R</i> _{free}	0.204/0.249 (0.229/0.236)
No. of atoms	
Protein (residues)	10,853 (1,392 residues)
Ligand/additive	30
Water	877
Mean <i>B</i> -factors (Å ²)	
Protein	80.5
Ligand/additive	61.1
Water	74.2
R.m.s. deviations	
Bond lengths (Å)	0.008
Bond angles (°)	1.090

794 Values in parentheses are for highest-resolution shell. Each dataset was collected from a single-crystal.

795
 796
 797
 798

799 **Table 1 (continued). Cryo-electron microscopy data collection and refinement statistics**

DCAF15-DDB1-DDA1- RBM39(RRM2)-Indisulam	
Data collection and processing	
Magnification	130,000 (K2-Gatan camera)
Voltage (keV)	300
Electron exposure (e-/Å ²)	40
Defocus range (µm)	-0.8 – -2.0
Pixel size (Å)	0.86
Symmetry imposed	C1
Initial particle images	415,203
Final particle images	126,974
Map resolution (Å)	3.54
FSC threshold	0.143
Map resolution range (Å)	12.0-3.54
Refinement	
Initial model used (PDB code)	Multiple models
Resolution (Å)	3.54
FSC threshold	0.143
Resolution range (Å)	30.0-3.54
Map sharpening B-factor (Å ²)	119
No. of atoms	
Protein (residues)	10,324 (1,308 residues)
Ligand/ion	24
Water	0
Mean B factors (Å ²)	
Protein	73.40
Ligand	102.42
R.m.s. deviations	
Bond lengths (Å)	0.007
Bond angles (°)	0.985

800

801

802 *Differential scanning fluorimetry*

803 Thermal shift assays were performed with 5 µM of purified DCAF15-DDB1-DDA1 or
804 DCAF15-DDB1 complex in buffer D (see purification protocol). The samples were
805 mixed with 5x SYPRO Orange (Molecular Probes) prior to the thermal cycle. The
806 temperature was ramped from 4 to 95 °C in a ViiA7 real-time PCR machine (Applied
807 Biosystems). The protein melting temperature, *T_m*, was calculated based on the
808 resulting fluorescence data using curve-fitting to a Boltzmann function by the Protein
809 Thermal Shift software version 1.1 (Life Technologies). The standard deviation was
810 calculated by comparing three replicate experiments. Data were plotted using
811 GraphPad Prism 8.

812 *Cell culture*

813 HCT116 and HEK293T cells were obtained by ATCC. HCT-116 cells were maintained
814 in McCoy's 5A and HEK293T were maintained in DMEM (Invitrogen), both media
815 supplemented with 10% (v:v) FBS, 1% (w:v) penicillin-streptomycin, and 2 mM L-
816 glutamine (VWR) in a humidified incubator held at 37°C and 5% CO₂. Cells were
817 confirmed to be mycoplasma negative via MycoAlert™ Mycoplasma Detection Kit
818 (Lonza).

819

820 *Cell viability assays*

821 HCT116 or HEK293T cells were trypsinized, diluted in growth media to a final
822 concentration 2.5x10⁴ cells/mL, and plated in 384-well plates (Corning #3707) at 40
823 μL/well. Cells were incubated overnight at 37 °C (5% CO₂). Test compounds were
824 diluted to various concentrations in DMSO and further diluted 40X in growth media.
825 Cells were treated with 10 μL/well of diluted of test compound or vehicle (0.05% DMSO
826 final concentration) via BioMeK liquid handled and incubated for 72hrs at 37C
827 (5%CO₂).

828 After 72 hr incubation, treated cells were equilibrated to room temperature for 30 min.
829 CellTiter-Glo® reagent (Promega) was added at 20 μL per well and plates were placed
830 on an orbital shaker for 30 s prior to a 10 min incubation at room temperature.
831 Luminescence was measured using an Envision MultiLabel reader (200 ms read time).
832 Readings from all DMSO wells were averaged and each test well reading (compound
833 treated) was normalized to DMSO. Results were plotted in GraphPad Prism 8 and
834 data were fit using the nonlinear fit module (“3 parameter – log dose vs response”) to
835 determine IC₅₀.

836

837 *siRNA knockdown of DDA-1*

838 For siRNA transfection, 10⁶ cells plated per well of a 6-well plate were transfected with
839 150 pmol siRNAs (Ambion: Negative Control #AM4611, DDA1-2 Cat #4392420 ID
840 #s35423) using 9 uL of Lipofectamine RNAiMAX (Life Technologies). After 40 hours
841 post-transfection, cells were washed with PBS and re-suspended in DMEM, and then

842 treated with DMSO or Indisulam for another 24 hours before cell collection. Cells were
843 pelleted and washed with 2 x 1mL PBS and frozen at -80°C overnight and then thawed
844 and lysed with 100 µL of RIPA buffer (Thermo Scientific) supplemented with 1X HALT
845 protease inhibitor cocktail (Thermo Scientific).

846

847 *Western blotting and antibodies*

848 LDS samples were prepared using LDS sample buffer (Invitrogen, REF #NP0007) and
849 Sample Reducing Agent (Invitrogen, Cat #NP0009) and separated using Bio-Rad
850 PowerPac HC system using NUPAGE 4-12% Bis-Tris gels (Invitrogen, Cat
851 #NP0323BOX). Proteins were transferred via Bio-Rad Trans-Blot Turbo transfer
852 system onto Bio-Rad Trans-Blot turbo transfer pack with 0.2 µm nitrocellulose
853 membranes (Invitrogen, Cat #1704158).

854 Blots were incubated with primary antibody solutions made in TBS-T with 5% milk for
855 RBM39 (Sigma, Cat #HPA001591, 1:2500) GAPDH (CST, Cat #2118L, 1:1000),
856 Vinculin (Cell Signaling Technology, Cat# 13901S, 1:1000), ZNF277 (Pro-Sci, Cat
857 #46-616, 1:1000), RBM23 (Invitrogen, Cat# PA5-52060, 1:1000), or DDA1
858 (Proteintech, Cat #14995-1-AP, 1:1000) overnight at 4°C. Blots were then washed 3
859 x 5 mL TBS-T and incubated with secondary antibody (EMD Millipore, Cat #AP307P,
860 1:2500) for 1h at 25°C, then visualized with Amersham ECL (GE Life Sciences, Cat
861 #RPN2236) and imaged using Amersham Hyperfilm ECL (GE Life Sciences, Cat
862 #28906839).

863

864 *Fluorescence polarization assays*

865 To study the impact of various RBM39 substitutions on aryl sulfonamide-induced
866 recruitment to DCAF15, we leveraged the differential binding affinity of a FITC-labeled
867 Indisulam analog to DCAF15 complex-alone versus a DCAF15-RBM39 complex in a
868 fluorescence polarization assay.

869 We first determined the concentration of an Avi-DCAF15-DDB1-DDA1 complex
870 required to yield probe binding (high polarization) in the presence of RBM39(Δ150),
871 signaling ternary complex formation, and low probe binding (low polarization) in the

872 absence of RBM39(Δ 150). Avi-DCAF15/DDB1/DDA1 was diluted to 20 μ M in FP
873 Buffer, consisting of 20 mM HEPES pH 7.2, 150 mM NaCl, and 0.01% (v:v) Tween-
874 20, and serially diluted in the presence or absence of 2 μ M His-ZZ-RBM39(Δ 150).
875 Each mixture was dispensed into a black 384-well plate (Corning #3575) at 10 μ M per
876 well. Compound **9** (FITC-probe) was diluted to 40 nM in FP Buffer and dispensed at
877 10 μ L per well to yield a final concentration of 20 nM. Plates were incubated at room
878 temperature for 1 hr and read on an Envision MultiLabel reader equipped with
879 standard FITC-FP protocol/mirror sets. The Envision Assay Optimization Wizard was
880 used to adjust detector gain and to determine G-factor (measured on compound **9**-
881 only wells) for mP calculation.

882 To assess the impact of RBM39 mutation on ternary complex formation with DCAF15
883 and compound **9**, we titrated RBM39 variants in the presence of compound **9** and
884 DCAF15, measuring fluorescence polarization. Avi-DCAF15/DDB1/DDA1 and
885 compound **9** were diluted to 200 nM and 40 nM in FP buffer, respectively, and
886 dispensed into black 384-well plates (Corning #3575) at 10 μ L per well. RBM39
887 variants were diluted in FP buffer to 20 μ M each and serially diluted, with each mixture
888 then added at 10 μ L per well to yield final volume of 20 μ L. Plates were incubated at
889 room temperature for 1 hr and read on an Envision MultiLabel reader as before.

890

891 *TR-FRET recruitment assays*

892 In TR-FRET buffer consisting of 20 mM HEPES, pH 7.4, 150 mM NaCl, and 0.05%
893 (v:v) Triton X-100, a solution of 20 nM LanthaScreen™ Tb-Streptavidin (Thermo
894 Scientific, Cat# PV3965), 150 nM biotinylated-Avi-DCAF15/DDB1/DDA1, 500 nM
895 6XHis-ZZ-RBM39(Δ 150), and 50 nM anti-6xHis-FITC (AbCam, Cat# ab1206) was
896 prepared and transferred into a black, 384-well Corning plate (#3575) at 20 μ L per
897 well. DMSO stock solutions of various compounds and respective dilutions were
898 transferred acoustically via Echo 555 Liquid Handler (Labcyte, Inc) at 100 nL per well.
899 After transfer, plates were incubated at room temperature for 1 hr and TR-FRET was
900 read on the Envision Multi-label reader (using the following conditions).

901

902

Light source	Flash lamp
Top mirror	LANCE/DELFIA
Bottom mirror	N/A
Exc. filter	UV2 (TRF) 320
Using of excitation filter	Top
Ems. filter	Emission 520
Using of emission filter	Top
	Photometric
2nd ems. filter	492
Using of 2nd emission filter	Top
Measurement height	6.5 mm
Cycle	2000
Delay	60
Number of flashes	100
Number of flashes for 2nd detector	100
Number of sequence windows	1
Total time of windows	300
Excitation light	100%

903

904 TR-FRET ratios (520 nm /490 nm emission signals) were analyzed using Excel
905 (calculating averages and standard deviations) and these data were plotted in
906 GraphPad Prism 8.

907

908 *Proteome-wide motif search*

909 Given the complementarity between the RBM39(T262-P272) alpha helix, Indisulam,
910 and DCAF15 in the ternary complex, we queried the proteome for similar alpha
911 helicies, bearing residues critical for DCAF15-Indisulam binding, to identify additional

912 proteins that may be recruited to DCAF15. From described RBM39 mutagenesis
913 studies and previously published work^{17,18}, we determined residues M265, G268,
914 E271, and P272 to be most critical to DCAF15-Indisulam binding and established the
915 “X¹XXM⁴XXG⁷XXEP¹¹” motif as a putative degron. To identify compatible proteins with this
916 motif, we first accessed 20,407 unique human protein sequences from Uniprot
917 (www.uniprot.org), cataloging the availability of any associated x-ray/NMR structures
918 (6,475 entries). For proteins with available structures, we analyzed for the presence
919 of an alpha helix with a glycine residue and aligned this region on the alpha helix of
920 RBM39 in the ternary structure model with DCAF15. A backbone alpha carbon RMSD
921 of each protein structure versus the RBM39(RRM2) structure was calculated and if
922 the RMSD was <2Å (as in 3112 structures), we surveyed for steric clashes with
923 DCAF15. A steric clash of less than 10 heavy atoms between DCAF15 and the target
924 protein was considered acceptable. Proteins with low RMSD (<2Å) and minimal steric
925 clash to DCAF15 were considered. Finally, hit sequences were filtered by the
926 presence of the “X¹XXM⁴XXG⁷XXEP¹¹” sequence.

927

928 *Expression proteomics*

929 TMT-based expression proteomics was performed as previously described⁵⁹ with few
930 modifications. Indisulam-treated HCT116 cells (10⁶ cells treated with 10 uM Indisulam
931 for 4 hrs.) were harvested, washed 3 times with PBS, lysed with 500 µL lysis buffer
932 (8M Urea, 1% SDS, 50 mM Tris pH 8.5, with protease and phosphatase inhibitors
933 added), and then sonicated to shear DNA aggregates. After centrifugation, protein
934 concentrations were measured by Micro BCA™ Protein Assay Kit (Thermo
935 Cat#23235).

936 For each sample, 200 µg protein was aliquoted and reduced with 5 mM Dithiothreitol
937 (DTT) for 1 hr at room temperature (RT), alkylated with 15 mM iodoacetamide (IAA)
938 for 1 hr at RT in the dark, and then quenched with 10 mM DTT for 15 min at RT.
939 Alkylated proteins were purified via chloroform/methanol precipitation⁶⁰, dissolved in
940 denaturing buffer (8 M urea, 50 mM Tris, pH 8.5), and diluted with seven volumes of
941 50 mM Tris, pH 8.5. Protein was digested using Trypsin/Lys-C mix in an enzyme to
942 protein ratio of 1:25 and incubated overnight at 37 °C. A second digestion was

943 performed with additional Trypsin/Lys-C mix (enzyme to protein ratio of 1:50) for 4
944 hours.

945 The peptide sample was then desalted using a Water's tC18 SepPak plate (Waters
946 Cat# 186002321), dried down, and then resuspended in 100 μ L 0.1 M TEAB buffer,
947 pH 8.5. Peptide concentrations were determined using the Pierce™ Quantitative
948 Fluorometric Peptide Assay (Thermo Cat#23290) and normalized between samples
949 (~2 mg/mL)

950 For each sample, 200 μ g peptides were labeled via TMT10plex™ Isobaric Label
951 Reagent kit (Thermo Cat#90111) at the ratio of 4 units of TMT reagent to 1 unit of
952 peptide. TMT labeling efficiency was checked by running an MS analysis. Once the
953 labeling efficiency was confirmed to be greater than 99%, the reaction was quenched
954 with 0.5% with hydroxylamine for 15 min at RT. Equal amounts of each TMT-labeled
955 sample were combined, desalted using Water's tC18 SepPak plate (Waters
956 Cat#186002321), and then fractionated by HPLC - Waters XBridge C18 (3.5 μ m, 300
957 x 4.6 mm) column with gradient of 10-40% mobile phase B (90% acetonitrile with 5
958 mM ammonium formate, pH 10) in mobile phase A (5 mM ammonium formate, 2%
959 acetonitrile). Final fractionated peptide material was pooled into 24 fractions (~1-2 μ g
960 peptides/fraction).

961 Each fraction was analyzed using an Orbitrap Fusion™ Lumos™ Mass Spectrometer
962 (Thermo) equipped with a Reprosil-PUR column (1.9 μ m beads, 75 μ m ID x 15 μ m
963 tip x 20 cm, 120 Å). Samples were run using gradients of 7-28% mobile phase B (80%
964 acetonitrile with 0.1% formic acid) in mobile phase A (0.1% formic acid) using the SPS
965 MS3 mode. Thermo Proteome Discoverer™ was used to analyze raw data and
966 determine major cutoff parameters for peptide quantification (i.e. precursor
967 contamination <50%, minimum average reporter ion with signal/noise >10, and
968 peptide-spectrum match (PSM) \geq 1 for all peptides). Custom iPython notebook
969 processing with limma statistical analysis and normalization was used to determine
970 fold-changes and p-values between duplicate DMSO- and Indisulam-treated samples.
971 Specifically, the scipy.stats.f_oneway function was used to perform one-way ANOVA
972 and generate F-statistics and associate p-values from the F-distribution. Samples
973 were assumed to be independent, normally distributed, and homoscedastic.

974

975

976 *Chemical synthesis and characterization*

977 All chemical synthesis procedures and characterization data are provided in
978 Supplementary Note 2.

979

980 *Statistical Analysis*

981 All statistical analyses were performed using Prism 8 (GraphPad) unless otherwise
982 stated in the Methods section.

983

984 **Acknowledgments:** The authors thank M. Renatus for providing DCAF15 constructs
985 and M. Li for providing DDB1 and DDB1(Δ BPB) constructs. We also thank G. Pardee
986 for baculovirus generation and protein expression, S. Widger for additional expression
987 support, and X. Ma for helpful discussions on ligase structural biology. Finally, we
988 thank J. Bradner, J. Shulok, R. Jain, J. Porter, and J. Tallarico for helpful discussions
989 and input on this manuscript.

990

991 **Author contributions:** R.B., A.F., J.Z., B.O., S.J., and P.M. designed and/or
992 synthesized reported compounds. N.C., P.G., and H.V. performed crosslinking/mass-
993 spectrometry studies. A.B., D.K., A.G, performed surface plasmon resonance
994 experiments, while D.K. performed analytical ultracentrifugation. V.H. and R.G.K.
995 performed proteome-wide motif searches and structural/computational modelling.
996 C.B., H.S., and C.W. collected and processed Cryo-EM data. F.X. and J.C. conducted
997 expression proteomics experiments. A.O.F. and A.F. performed biological NMR
998 experiments. W.S. performed crystallographic screening and crystal optimization;
999 D.E.B. designed protein constructs, collected X-ray crystallography datasets, reduced
1000 data, determined initial crystal structures and refined final structures; M.K. refined final

1001 structures. L.X. purified DCAF15 complexes and RBM39 variants, and performed ITC
1002 and DSF experiments. J.P. and A.B. purified RBM39 variants, performed FP and TR-
1003 FRET assays, cellular viability assays, siRNA knockdown, and western blots. All
1004 authors contributed to writing. D.E.B., J.S., and J.P, wrote and edited the final
1005 manuscript. D.E.B., J.S., L.X., and J.P contributed intellectual and strategic input.

1006

1007 **Competing interests:** All authors are employees of Novartis, or were at the time of
1008 this study.

1009

1010 **Data availability:** The authors declare that the data supporting the findings of this
1011 study are available within the publication and its Supplementary Information files or
1012 have been deposited in the RCSB Protein Data Bank (PDB, <http://www.rcsb.org>) or
1013 Electron Microscopy Data Bank (EMDB, <http://www.ebi.ac.uk/pdbe/emdb/>), as
1014 appropriate. The PDB accession code for the human DCAF15-DDB1-DDA1-
1015 RBM39(RRM2)-Indisulam co-structure is ----. The EMDB accession code for the
1016 human DCAF15-DDB1-DDA1-RBM39(RRM2)-Indisulam co-structure is ----.

1017

1018 **References**

- 1019 1. Bondeson, D. P. & Crews, C. M. Targeted Protein Degradation by Small
1020 Molecules. *Annu. Rev. Pharmacol. Toxicol.* (2017). doi:10.1146/annurev-
1021 pharmtox-010715-103507
- 1022 2. Collins, I., Wang, H., Caldwell, J. J. & Chopra, R. Chemical approaches to
1023 targeted protein degradation through modulation of the ubiquitin–proteasome
1024 pathway. *Biochem. J.* (2017). doi:10.1042/bcj20160762
- 1025 3. Ciechanover, A. Intracellular protein degradation: From a Vague Idea, through
1026 the lysosome and the ubiquitin-proteasome system, and onto human diseases
1027 and drug targeting (Nobel Lecture). *Angewandte Chemie - International Edition*
1028 **44**, 5944–5967 (2005).

- 1029 4. Thrower, J. S. Recognition of the polyubiquitin proteolytic signal. *EMBO J.*
1030 (2000). doi:10.1093/emboj/19.1.94
- 1031 5. Yu, H. & Matouschek, A. Recognition of Client Proteins by the Proteasome.
1032 *Annu. Rev. Biophys.* (2017). doi:10.1146/annurev-biophys-070816-033719
- 1033 6. Finley, D., Chen, X. & Walters, K. J. Gates, Channels, and Switches: Elements
1034 of the Proteasome Machine. *Trends in Biochemical Sciences* (2016).
1035 doi:10.1016/j.tibs.2015.10.009
- 1036 7. Neutzner, M. & Neutzner, A. Enzymes of ubiquitination and deubiquitination.
1037 *Essays Biochem.* (2012). doi:10.1042/bse0520037
- 1038 8. Zheng, N. & Shabek, N. Ubiquitin Ligases: Structure, Function, and
1039 Regulation. *Annu. Rev. Biochem.* (2017). doi:10.1146/annurev-biochem-
1040 060815-014922
- 1041 9. Wu, Y. L. *et al.* Structural basis for an unexpected mode of SERM-Mediated
1042 ER antagonism. *Mol. Cell* (2005). doi:10.1016/j.molcel.2005.04.014
- 1043 10. Patel, H. K. & Bihani, T. Selective estrogen receptor modulators (SERMs) and
1044 selective estrogen receptor degraders (SERDs) in cancer treatment.
1045 *Pharmacology and Therapeutics* (2018).
1046 doi:10.1016/j.pharmthera.2017.12.012
- 1047 11. Neklesa, T. K., Winkler, J. D. & Crews, C. M. Targeted protein degradation by
1048 PROTACs. *Pharmacology and Therapeutics* (2017).
1049 doi:10.1016/j.pharmthera.2017.02.027
- 1050 12. Larrieu, A. & Vernoux, T. Comparison of plant hormone signalling systems.
1051 *Essays Biochem.* (2015). doi:10.1042/bse0580165
- 1052 13. Tan, X. *et al.* Mechanism of auxin perception by the TIR1 ubiquitin ligase.
1053 *Nature* (2007). doi:10.1038/nature05731
- 1054 14. Chamberlain, P. P. & Cathers, B. E. Cereblon modulators: Low molecular
1055 weight inducers of protein degradation. *Drug Discovery Today: Technologies*
1056 (2019). doi:10.1016/j.ddtec.2019.02.004
- 1057 15. Supuran, C. T. Indisulam: an anticancer sulfonamide in clinical development.
1058 *Expert Opin. Investig. Drugs* (2003). doi:10.1517/eoid.12.2.283.21409
- 1059 16. Ozawa, Y. *et al.* E7070, a novel sulphonamide agent with potent antitumour
1060 activity in vitro and in vivo. *Eur. J. Cancer* (2001). doi:10.1016/S0959-
1061 8049(01)00275-1
- 1062 17. Uehara, T. *et al.* Selective degradation of splicing factor CAPER α by

- 1063 anticancer sulfonamides. *Nat. Chem. Biol.* (2017). doi:10.1038/nchembio.2363
- 1064 18. Han, T. *et al.* Anticancer sulfonamides target splicing by inducing RBM39
1065 degradation via recruitment to DCAF15. *Science* (80-.). (2017).
1066 doi:10.1126/science.aal3755
- 1067 19. Laskowski, R. A., Jabłońska, J., Pravda, L., Vařeková, R. S. & Thornton, J. M.
1068 PDBsum: Structural summaries of PDB entries. *Protein Sci.* **27**, 129–134
1069 (2018).
- 1070 20. Holm, L. & Rosenström, P. Dali server: conservation mapping in 3D. *Nucleic
1071 Acids Res.* **38**, W545–W549 (2010).
- 1072 21. Dias, J. *et al.* Structural analysis of the KANSL1/WDR5/ KANSL2 complex
1073 reveals that WDR5 is required for efficient assembly and chromatin targeting of
1074 the NSL complex. *Genes Dev.* (2014). doi:10.1101/gad.240200.114
- 1075 22. Wysocka, J. *et al.* WDR5 associates with histone H3 methylated at K4 and is
1076 essential for H3 K4 methylation and vertebrate development. *Cell* (2005).
1077 doi:10.1016/j.cell.2005.03.036
- 1078 23. Song, J. J. & Kingston, R. E. WDR5 interacts with mixed lineage leukemia
1079 (MLL) protein via the histone H3-binding pocket. *J. Biol. Chem.* (2008).
1080 doi:10.1074/jbc.M806900200
- 1081 24. Qu, Q. *et al.* Structure and Conformational Dynamics of a COMPASS Histone
1082 H3K4 Methyltransferase Complex. *Cell* **174**, 1117–1126.e12 (2018).
- 1083 25. Jain, B. P. & Pandey, S. WD40 Repeat Proteins: Signalling Scaffold with
1084 Diverse Functions. *Protein J.* **37**, 391–406 (2018).
- 1085 26. Xue, B., Dunbrack, R. L., Williams, R. W., Dunker, A. K. & Uversky, V. N.
1086 PONDR-FIT: a meta-predictor of intrinsically disordered amino acids. *Biochim.
1087 Biophys. Acta* **1804**, 996–1010 (2010).
- 1088 27. Wu, Y. *et al.* The DDB1–DCAF1–Vpr–UNG2 crystal structure reveals how HIV-
1089 1 Vpr steers human UNG2 toward destruction. *Nat. Struct. Mol. Biol.* **23**, 933–
1090 940 (2016).
- 1091 28. Scrima, A. *et al.* Structural Basis of UV DNA-Damage Recognition by the
1092 DDB1-DDB2 Complex. *Cell* (2008). doi:10.1016/j.cell.2008.10.045
- 1093 29. Fischer, E. S. *et al.* Structure of the DDB1-CRBN E3 ubiquitin ligase in
1094 complex with thalidomide. *Nature* (2014). doi:10.1038/nature13527
- 1095 30. Shabek, N. *et al.* Structural insights into DDA1 function as a core component
1096 of the CRL4-DDB1 ubiquitin ligase. *Cell Discov* **4**, 67–67 (2018).

- 1097 31. Chambers, J. C., Kenan, D., Martin, B. J. & Keene, J. D. Genomic structure
1098 and amino acid sequence domains of the human La autoantigen. *J. Biol.*
1099 *Chem.* **263**, 18043–51 (1988).
- 1100 32. Dreyfuss, G., Swanson, M. S. & Piñol-Roma, S. Heterogeneous nuclear
1101 ribonucleoprotein particles and the pathway of mRNA formation. *Trends*
1102 *Biochem. Sci.* **13**, 86–91 (1988).
- 1103 33. Murray, J. M. & Bussiere, D. E. Targeting the Purinome. in *Methods in*
1104 *molecular biology (Clifton, N.J.)* **575**, 47–92 (2009).
- 1105 34. Molecular Operating Environment (MOE), 2013.08. Molecular Operating
1106 Environment (MOE), 2013.08; Chemical Computing Group Inc., 1010
1107 Sherbooke St. West, Suite #910, Montreal, QC, Canada, H3A 2R7. *Mol. Oper.*
1108 *Environ. (MOE), 2013.08; Chem. Comput. Gr. Inc., 1010 Sherbooke St. West,*
1109 *Suite #910, Montr. QC, Canada, H3A 2R7, 2013.* (2016).
- 1110 35. Milletti, F., Storchi, L., Sforza, G. & Cruciani, G. New and original pKa
1111 prediction method using grid molecular interaction fields. *J. Chem. Inf. Model.*
1112 (2007). doi:10.1021/ci700018y
- 1113 36. Chardin, P. & McCormick, F. Brefeldin A: The advantage of being
1114 uncompetitive. *Cell* (1999). doi:10.1016/S0092-8674(00)80724-2
- 1115 37. Huh, K. *et al.* Human Papillomavirus Type 16 E7 Oncoprotein Associates with
1116 the Cullin 2 Ubiquitin Ligase Complex, Which Contributes to Degradation of
1117 the Retinoblastoma Tumor Suppressor. *J. Virol.* (2007). doi:10.1128/jvi.00881-
1118 07
- 1119 38. Martinez-Zapien, D. *et al.* Structure of the E6/E6AP/p53 complex required for
1120 HPV-mediated degradation of p53. *Nature* (2016). doi:10.1038/nature16481
- 1121 39. Poirson, J. *et al.* Mapping the interactome of HPV E6 and E7 oncoproteins with
1122 the ubiquitin-proteasome system. *FEBS Journal* (2017).
1123 doi:10.1111/febs.14193
- 1124 40. Pick, E. *et al.* Mammalian DET1 Regulates Cul4A Activity and Forms Stable
1125 Complexes with E2 Ubiquitin-Conjugating Enzymes. *Mol. Cell. Biol.* (2007).
1126 doi:10.1128/mcb.02432-06
- 1127 41. Olma, M. H. *et al.* An interaction network of the mammalian COP9
1128 signalosome identifies Dda1 as a core subunit of multiple Cul4-based E3
1129 ligases. *J. Cell Sci.* (2009). doi:10.1242/jcs.043539
- 1130 42. Gao, S. *et al.* Activation of c-Abl kinase potentiates the anti-myeloma drug

- 1131 lenalidomide by promoting DDA1 protein recruitment to the CRL4 ubiquitin
1132 ligase. *J. Biol. Chem.* (2017). doi:10.1074/jbc.M116.761551
- 1133 43. Zhu, Y. X. *et al.* Identification of cereblon-binding proteins and relationship with
1134 response and survival after IMiDs in multiple myeloma. *Blood* (2014).
1135 doi:10.1182/blood-2014-02-557819
- 1136 44. Krönke, J. *et al.* Lenalidomide causes selective degradation of IKZF1 and
1137 IKZF3 in multiple myeloma cells. *Science* (80-.). (2014).
1138 doi:10.1126/science.1244851
- 1139 45. Sievers, Q. L. *et al.* Defining the human C2H2 zinc finger degrome targeted by
1140 thalidomide analogs through CRBN. *Science* (80-.). (2018).
1141 doi:10.1126/science.aat0572
- 1142 46. Petzold, G., Fischer, E. S. & Thomä, N. H. Structural basis of lenalidomide-
1143 induced CK1 α degradation by the CRL4 CRBN ubiquitin ligase. *Nature* (2016).
1144 doi:10.1038/nature16979
- 1145 47. Matyskiela, M. E. *et al.* A novel cereblon modulator recruits GSPT1 to the
1146 CRL4 CRBN ubiquitin ligase. *Nature* (2016). doi:10.1038/nature18611
- 1147 48. Laue, T. M., Shah, B. D., Ridgeway, T. M. & Pelletier, S. L. Computer-aided
1148 interpretation of analytical sedimentation data for proteins. in *Analytical*
1149 *ultracentrifugation in biochemistry and polymer science* (1992).
- 1150 49. Schuck, P. Size-distribution analysis of macromolecules by sedimentation
1151 velocity ultracentrifugation and Lamm equation modeling. *Biophys. J.* (2000).
1152 doi:10.1016/S0006-3495(00)76713-0
- 1153 50. Mayer, M. & Meyer, B. Group epitope mapping by saturation transfer
1154 difference NMR to identify segments of a ligand in direct contact with a protein
1155 receptor. *J. Am. Chem. Soc.* (2001). doi:10.1021/ja0100120
- 1156 51. Bhunia, A., Bhattacharjya, S. & Chatterjee, S. Applications of saturation
1157 transfer difference NMR in biological systems. *Drug Discovery Today* (2012).
1158 doi:10.1016/j.drudis.2011.12.016
- 1159 52. Combe, C. W., Fischer, L. & Rappsilber, J. xiNET: Cross-link Network Maps
1160 With Residue Resolution. *Mol. Cell. Proteomics* (2015).
1161 doi:10.1074/mcp.o114.042259
- 1162 53. Adams, P. D. *et al.* PHENIX: A comprehensive Python-based system for
1163 macromolecular structure solution. *Acta Crystallogr. Sect. D Biol. Crystallogr.*
1164 (2010). doi:10.1107/S09074444909052925

- 1165 54. Blanc, E. *et al.* Refinement of severely incomplete structures with maximum
1166 likelihood in BUSTER-TNT. *Acta Crystallogr. Sect. D Biol. Crystallogr.* (2004).
1167 doi:10.1107/S0907444904016427
- 1168 55. Chen, V. B. *et al.* *MolProbity*: all-atom structure validation for macromolecular
1169 crystallography. *Acta Crystallogr. Sect. D Biol. Crystallogr.* **66**, 12–21 (2010).
- 1170 56. Grant, T., Rohou, A. & Grigorieff, N. Cistem, user-friendly software for single-
1171 particle image processing. *Elife* (2018). doi:10.7554/eLife.35383
- 1172 57. Zivanov, J. *et al.* New tools for automated high-resolution cryo-EM structure
1173 determination in RELION-3. *Elife* (2018). doi:10.7554/eLife.42166
- 1174 58. Emsley, P., Lohkamp, B., Scott, W. G. & Cowtan, K. Features and
1175 development of Coot. *Acta Crystallogr. Sect. D Biol. Crystallogr.* (2010).
1176 doi:10.1107/S0907444910007493
- 1177 59. Erb, M. A. *et al.* Transcription control by the ENL YEATS domain in acute
1178 leukaemia. *Nature* (2017). doi:10.1038/nature21688
- 1179 60. Wessel, D. & Flüggé, U. I. A method for the quantitative recovery of protein in
1180 dilute solution in the presence of detergents and lipids. *Anal. Biochem.* (1984).
1181 doi:10.1016/0003-2697(84)90782-6
1182

Figure 1: Purification and functional validation of RBM39 and DCAF15-DDB1-DDA1 complex

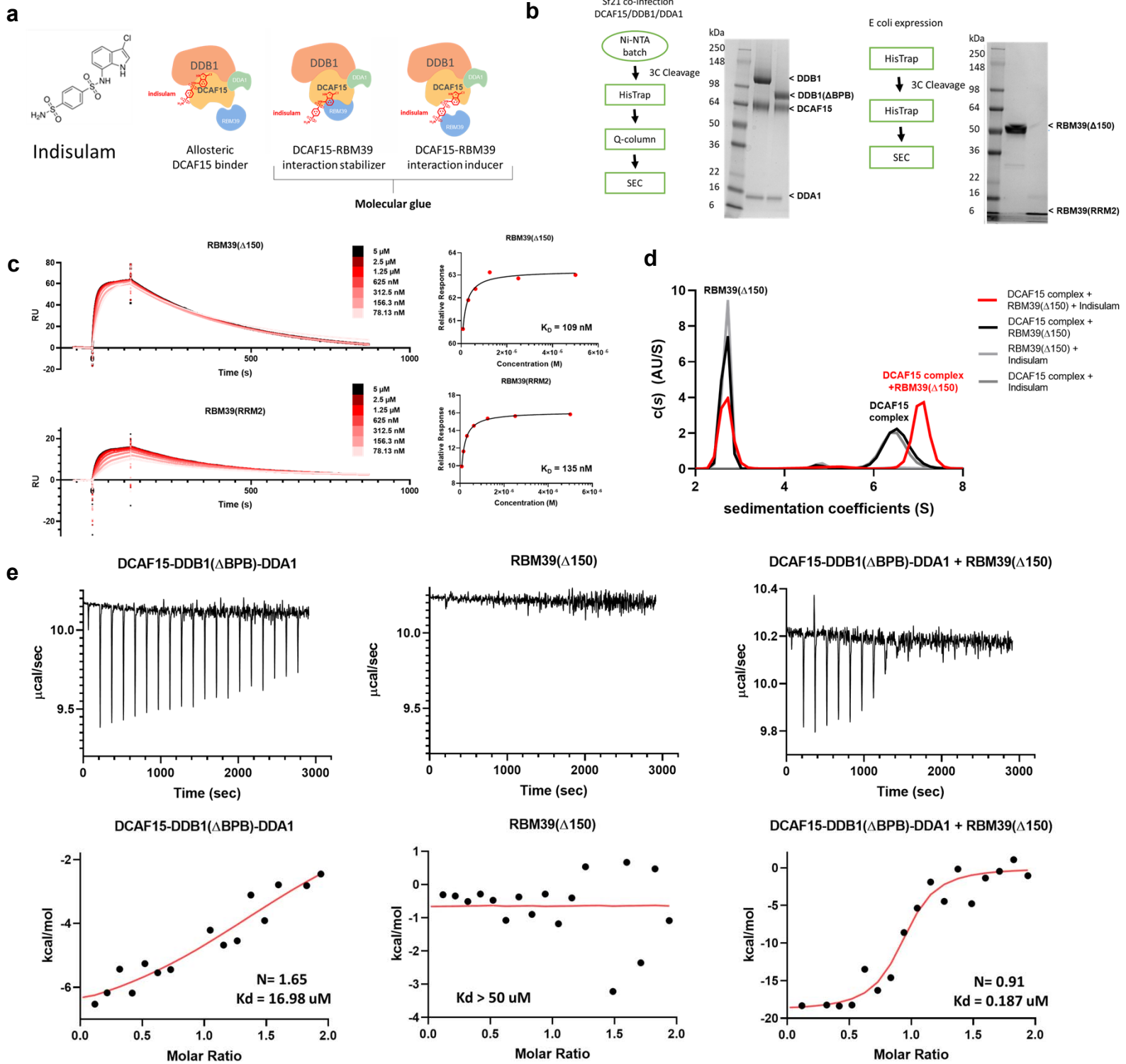


Figure 1: Purification and functional validation of RBM39 and DCAF15-DDB1-DDA1 complexes. **a**, Structure of Indisulam and representations of potential mechanisms of action for Indisulam-mediated recruitment of RBM39 to DCAF15. **b**, Expression systems, purification workflows, and Coomassie-stained gels for DCAF15-DDB1-DDA1, DCAF15-DDB1(ΔBPB)-DDA1 (left), RBM39(Δ150), and RBM39(RRM2) (right) proteins. **c**, Surface plasmon resonance (SPR) data characterizing Indisulam-mediated interaction between purified DCAF15-DDB1-DDA1 and RBM39 proteins. Biotinylated-DCAF15-DDB1-DDA1 was captured on the surface of SA chip and response was measured following injection of varied concentrations of RBM39(Δ150) (top) or RBM39(RRM2) (bottom) in the presence of 20 μM Indisulam. This experiment was repeated two independent times with representative data shown. **d**, Analytical ultracentrifugation (AUC) analysis of the interaction between 2.5 μM DCAF15-DDB1(ΔBPB)-DDA1 (DCAF15 complex) and 10 μM His-ZZ-RBM39(Δ150) in presence (red line) and absence (black line) of Indisulam. This experiment was repeated two independent times with representative data shown. **e**, Isothermal calorimetry measurements on 50 μM DCAF15-DDB1(ΔBPB)-DDA1 (left), 50 μM RBM39(Δ150) (middle), and a mixture of 10 μM both proteins (right) upon injections of 500 μM or 100 μM Indisulam. Corresponding fits reveal K_d measurements for Indisulam to be 17 μM for DCAF15-DDB1(ΔBPB)-DDA1 alone, >50 μM for RBM39(Δ150) alone, and 187 nM for DCAF15-DDB1(ΔBPB)-DDA1 and RBM39(Δ150) mixture. Representative data shown from an experiment performed two independent times and once for DCAF15-DDB1(ΔBPB)-DDA1-Indisulam experiment.

Figure 2: Structural analysis of the human DCAF15-DDB1-DDB1-DDA1-RBM39(RRM2) complex with Indisulam

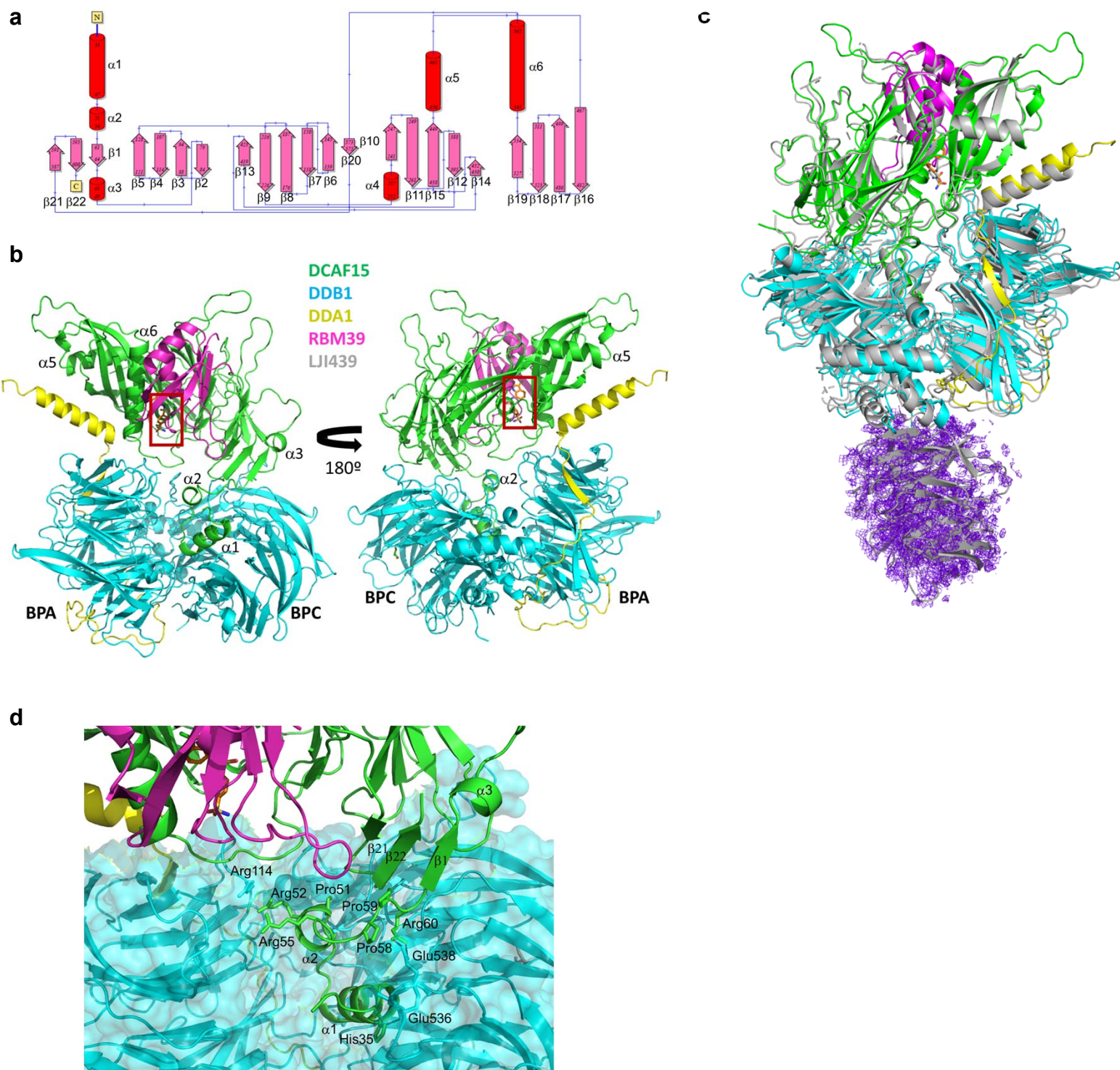


Figure 2: Structural analysis of the human DCAF15-DDB1-DDB1-DDA1-RBM39(RRM2) complex with Indisulam. **a**, Secondary structure and connectivity diagram for DCAF15. Residues 1-31, 272-385, and 398-416 are disordered and are not visible in electron density maps. The N- and C-terminus are labelled. **b**, Overall quaternary structure of human DCAF15-DDB1(ΔBPB)-DDA1-RBM39(RRM2) in complex with Indisulam. DCAF15 is shown in green, DDB1 in blue, DDA1 in yellow, and RBM39(RRM2) in magenta. The Indisulam binding site between DCAF15 and RBM39(RRM2) is boxed in red. Two views separated by 180° are presented. Key structural elements on DCAF15 are labelled, as are the BPA and BPC domains on DDB1. **c**, The cryo-EM structure of human DCAF15-DDB1(ΔBPB)-DDA1-RBM39(RRM2) in complex with Indisulam overlapped with the X-ray co-structure. The cryo-EM co-structure is shown in grey. **d**, Helix-loop-helix docking interactions with DDB1 and the 'arginine ladder'. The helix-loop-helix comprising α1 and α2 is shown docking to DDB1. Key hydrogen-bonding interactions are shown as dotted lines. Key hydrophobic residues are also shown. The unusual 'arginine ladder' comprised of Arg52 and Arg55 from DCAF15 and Arg114 from DDB1 is also shown, as are portions of DDA1, RBM39(RRM2), and Indisulam

Figure 3 : DDA-1 stabilizes the DCAF15-DDB1 complex and impacts degradation of RBM39 by Indisulam

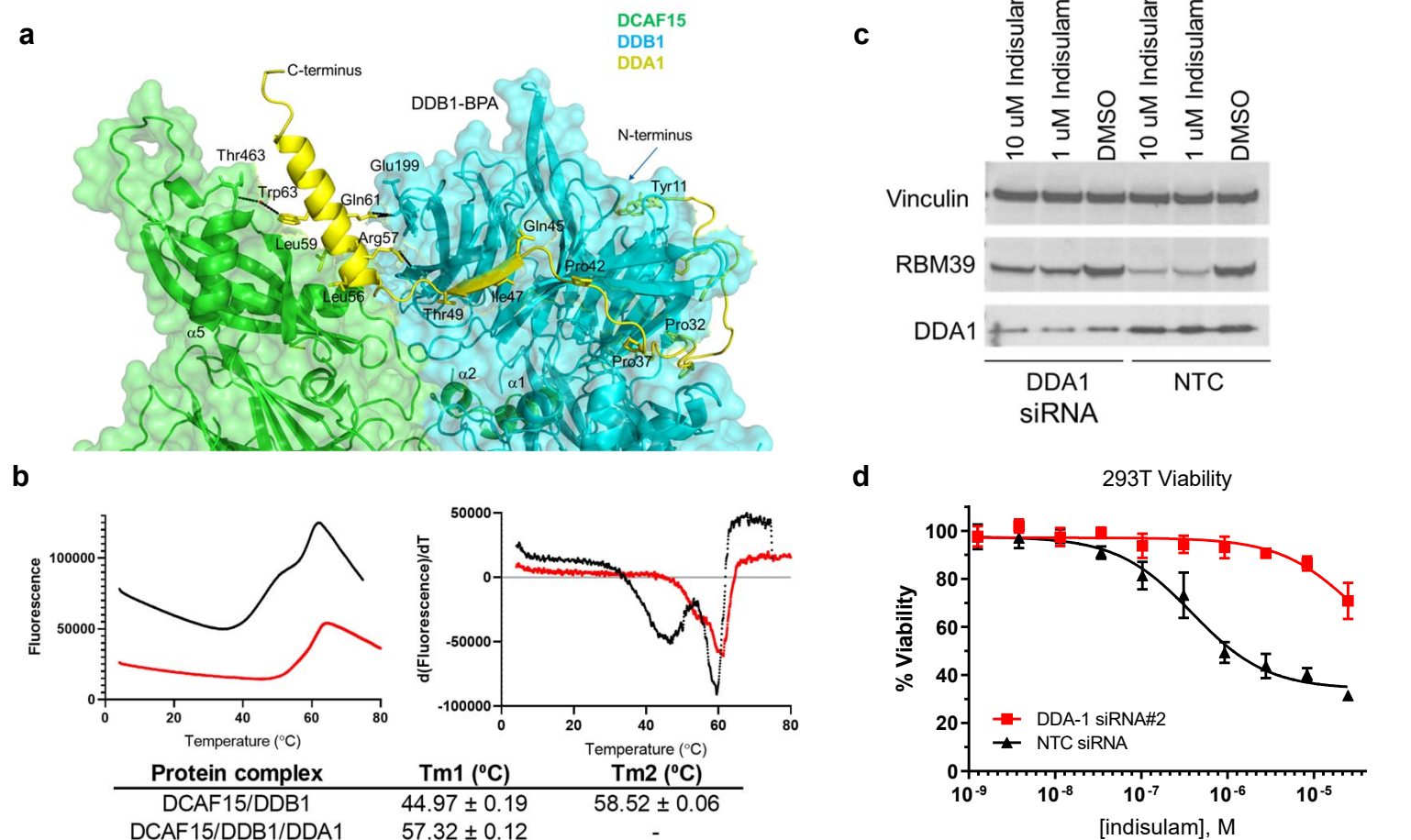


Figure 3: DDA1 stabilizes the DCAF15-DDB1 complex and impacts degradation of RBM39 by Indisulam. **a**, Interactions between DDA1(yellow), DCAF15 (green), and DDB1 (blue). Key residues are labelled and key salt-bridges and hydrogen-bonding interactions are shown as dotted lines. Residues on DDA1 which line the interaction surface for DDB1 are labelled. Within the β -sheet portion of DDA1, hydrogen-bond patterns similar to parallel β -sheet hydrogen-bonding exist. The N- and C-terminus of DDA1 are identified. **b**, Differential scanning fluorimetry (DSF) analysis measuring thermal stability of purified DCAF15-DDB1 (5 μ M) (black lines) and DCAF15-DDB1-DDA1 (5 μ M) (red lines) complexes. Both raw fluorescence (left) and $-d(\text{fluorescence})/d(\text{temperature})$ (right) were plotted over temperature. Plotted data represent the median value for three ($n=3$) biological replicates from one individual experiment. Tabular Tm values are listed \pm s.d. of the mean for the same three ($n=3$) biological replicates. **c**, Western blots showing levels of RBM39 in HEK293T cells transfected with DDA1 siRNA or a non-targeting control following 6 h treatment of 10 μ M Indisulam, 1 μ M Indisulam, or DMSO. Data shown from one individual, representative experiment from three independent repeats. **d**, Effect of 72 h Indisulam treatment on viability (CellTiterGlo) of HEK293T cells transfected with DDA1 siRNA (red line) or a non-targeting control (black line). Error bars represent s.d. of the mean from four biological replicates ($n=4$) in a single experiment. Each experiment was performed two independent times.

Figure 4: Detailed description of Indisulam binding at the DCAF15 and RBM39 interface

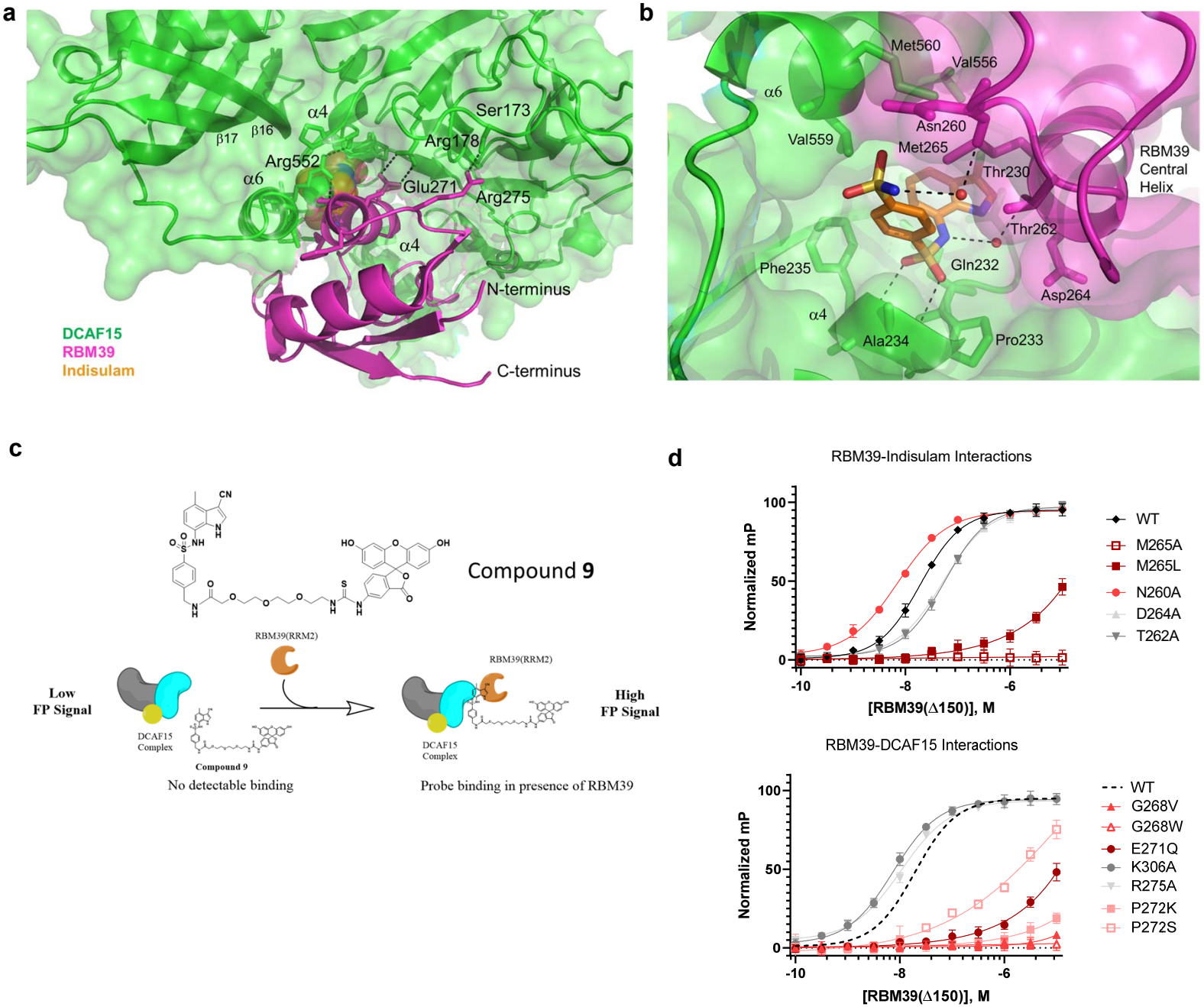


Figure 4: Detailed description of Indisulam binding at the DCAF15 and RBM39 interface. **a**, Non-Indisulam mediated interactions between DCAF15 (green) and RBM39 (magenta). Enthalpic interactions are shown as dotted lines. The majority of the interaction is due to shape complementarity and non-polar interactions, with interspersed electrostatic interactions and hydrogen-bonding. The N- and C-terminus of RBM39 are identified. **b**, Indisulam-mediated interactions between DCAF15 and RBM39. Indisulam (orange) bridges the structure of DCAF15 (green) and RBM39 (magenta) by forming several direct or water-mediated interactions with both DCAF15 and RBM39 and serves to increase the complementarity between the two surfaces. Hydrogen-bonds are shown as dotted lines and the surfaces of both DCAF15 and RBM39 are shown. Key residues are labelled. **c**, Schematic illustrating FP assay used to measure ternary complex formation between DCAF15-DDB1-DDA1, RBM39(Δ 150) variants, and a FITC-labeled Indisulam analog **9**. 100 nM of DCAF15 complex is insufficient to bind **9** in the absence of RBM39(Δ 150) and generates a low FP signal. In the presence of increasing concentrations of RBM39(Δ 150) a ternary complex forms and FP signal increases. Protein titration data is described in Supplementary Fig. 9. **d**, FP assay measuring ternary complex formation between DCAF15-DDB1-DDA1 and RBM39(Δ 150) variants bearing mutations at residues mediating direct and water-mediated interactions with Indisulam (top) or DCAF15 (bottom). Error bars represent s.d. of the mean from eight biological replicates ($n=8$) in a single experiment. Dotted line in right graph represents nonlinear data fit from wild-type RBM39(Δ 150) data shown in left graph. Each experiment was repeated three independent times. Characterization data for all RBM39 variants are included in Supplementary Fig. 10

Figure 5: Structure-activity relationships for Indisulam as measured by DCAF15/DDA1/DDA1-RBM39 recruitment assay

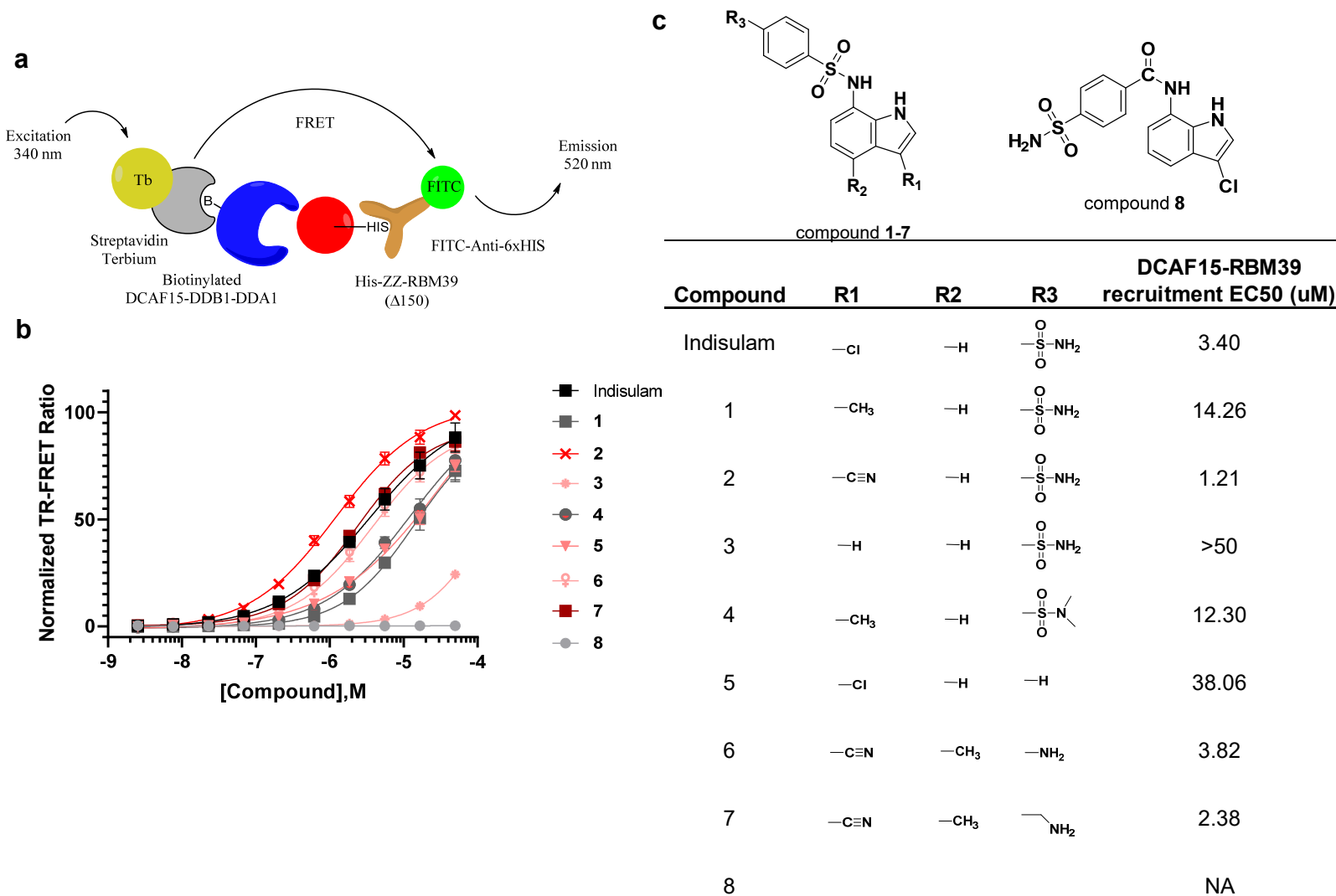


Figure 5: Structure-activity relationships for Indisulam as measured by DCAF15-DDB1-DDA1-RBM39 recruitment assay. **a**, Schematic illustrating time-resolved fluorescence energy transfer (TR-FRET) assay used to measure compound-induced recruitment of RBM39(Δ150) to DCAF15-DDB1-DDA1. Biotinylated DCAF15-DDB1-DDA1 complex was labeled with streptavidin-terbium conjugate to act as fluorescent donor to a FITC-antibody conjugate bound to his-tagged RBM39(Δ150). Upon ternary complex formation, TR-FRET signal is measured and reported as a ratio between emissions at 340 nm and 520 nm. **b**, DMSO-normalized TR-FRET ratios measured for varied doses of Indisulam (black line) and analogs in DCAF15-DDB1-DDA1-RBM39 recruitment assay. Error bars represent s.d. of the mean from four biological replicates (n=4) in a single experiment. **c**, Structure-activity relationship table describing generalized structures for analogs included (top) and impact of various substituents on DCAF15-DDB1-DDA1-RBM39 recruitment as described by EC₅₀ values in TR-FRET assay (bottom).

Figure 6: Proteome-wide motif search predicts molecular basis for Indisulam selectivity

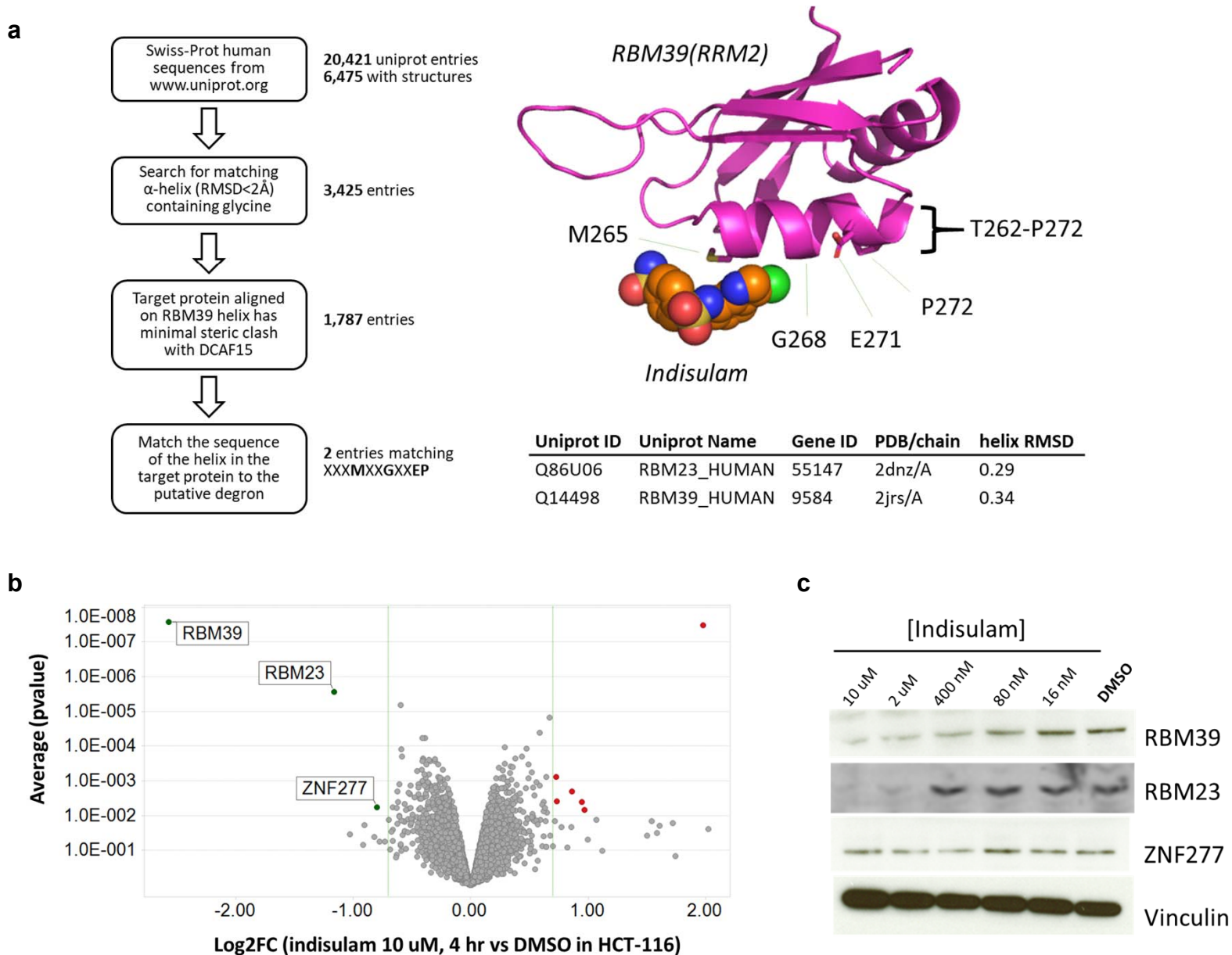
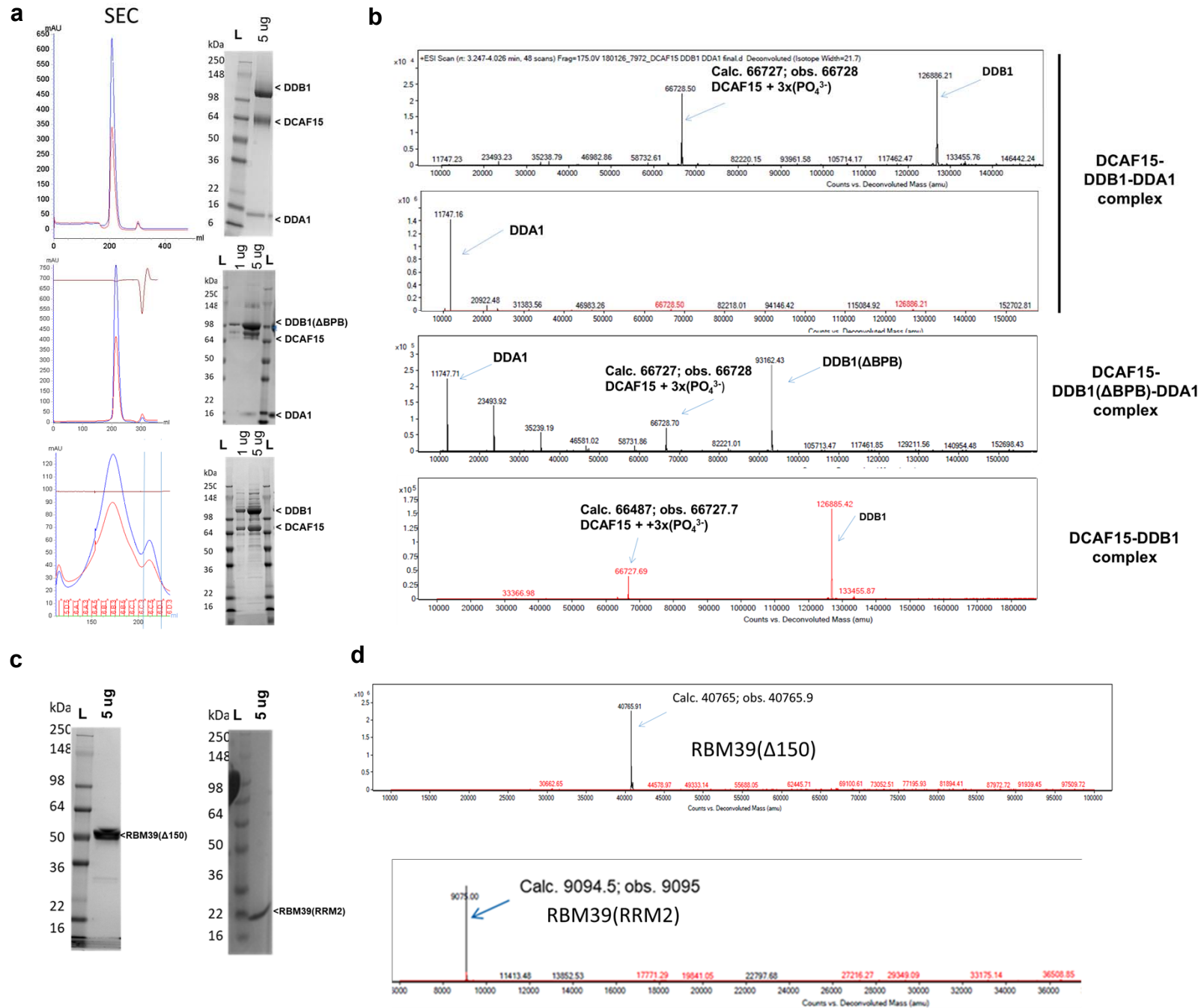


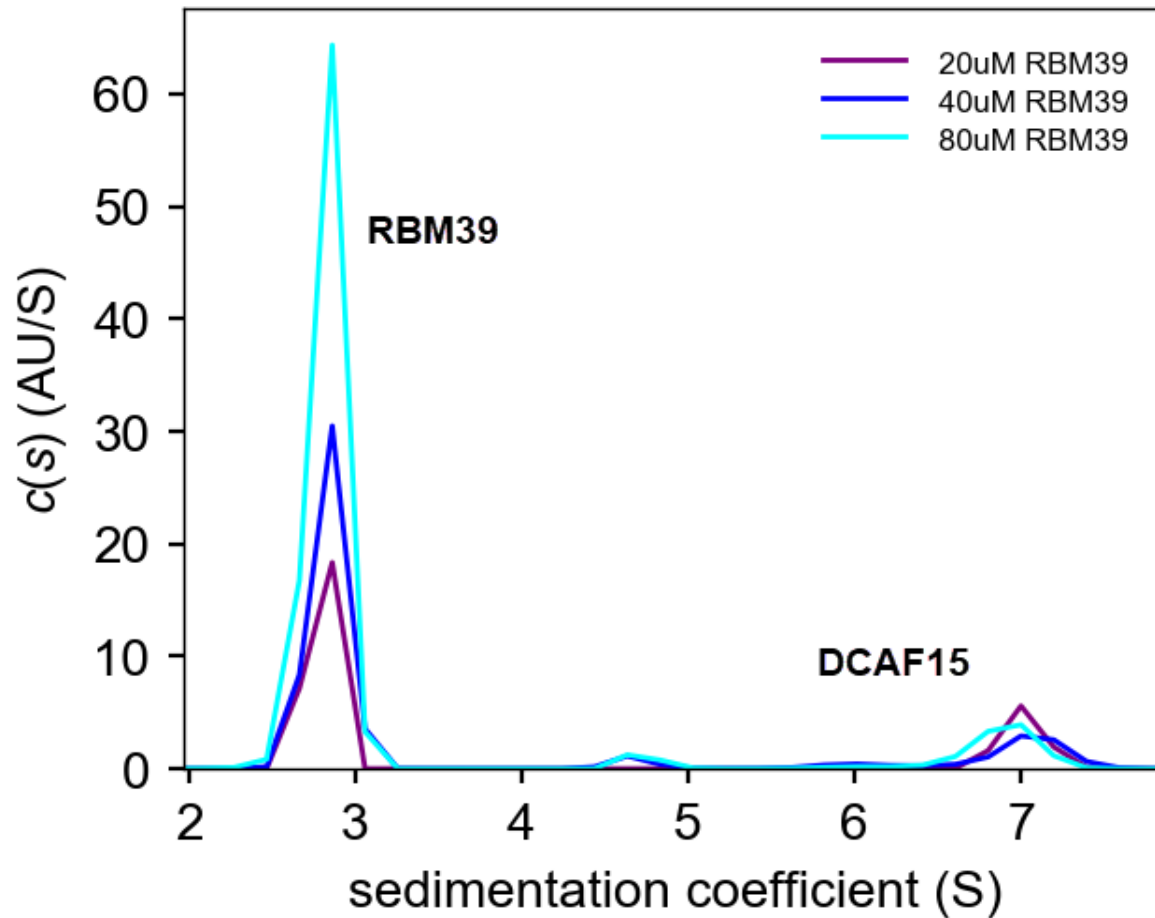
Figure 6: Proteome-wide motif search predicts Indisulam selectivity confirmed by expression proteomics. **a**, Bioinformatics workflow for identifying proteins bearing putative degron motif required for DCAF15-Indisulam recruitment (left) and structures of DCAF15-bound Indisulam (orange) and RBM39(RRM2) (magenta) with central alpha helix highlighted (right). The RBM39 residues found to be most critical for DCAF15-Indisulam recruitment are labeled (M265, G268, E271, and P272). 6,475 proteins with known structures were identified in the Swiss-Prot database, of which 3,425 had a glycine in an alpha helix. 3,112 of the glycine-containing alpha helices aligned to an RBM39(RRM2) structure (2JRS) with RMSD < 2.0 Å. Among these matches, only RBM23 and RBM39 helices had a sequence matching the required X'XXM⁴XXG⁷XXEP¹¹ motif. RMSD values, PDB IDs, and gene names shown in bottom table. **b**, Volcano plot summary of expression proteomics experiments comparing lysates from HCT-116 cells treated for 4 h with 10 μ M Indisulam or DMSO. Significant downregulated proteins (p value < 1E-2, Log₂ fold-change) are labeled. Data represents two (n=2) biological replicates per treatment condition in a single experiment. **c**, Western blots showing levels of RBM39, RBM23, and ZNF277 in HCT116 cells following 4 h treatment with varied concentrations of Indisulam or DMSO. Data shown from one individual, representative experiment from three independent repeats.

Supplementary Figure 1 : Characterization of purified RBM39 and DCAF15/DDB1/DDA1 complexes



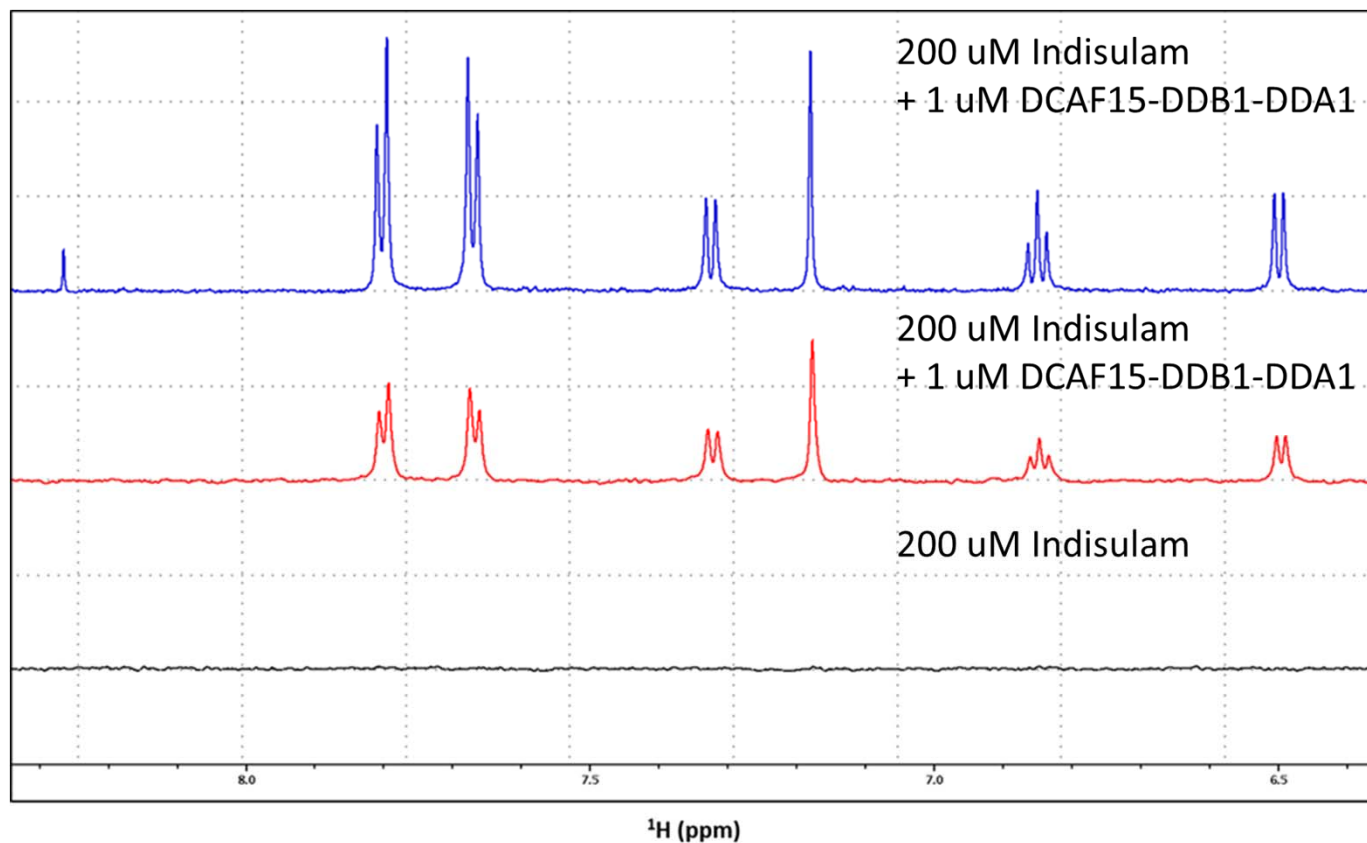
Supplementary Figure 1: Characterization of purified RBM39 and DCAF15-DDB1-DDA1 complexes. **a**, Size-exclusion chromatography (SEC) traces (absorbance at 280 nm) from GE Superdex 200 column separation of purified DCAF15-DDB1-DDA1 (top), DCAF15-DDB1(ΔBPB)-DDA1 (middle), and DCAF15-DDB1 (bottom) samples alongside Coomassie-stained SDS-PAGE analysis. **b**, LC-MS analysis and mass determination for purified DCAF15-DDB1-DDA1 (top), DCAF15-DDB1(ΔBPB)-DDA1 (middle), and DCAF15-DDB1 (bottom) samples. **c**, Coomassie-stained gels for RBM39(Δ150) and RBM39(RRM2) proteins (left and right, respectively) and **d**, associated LC-MS analysis to confirm masses (top and bottom, respectively)

Supplementary Figure 2 : Recruitment of RBM39 to DCAF15 is Indisulam-Dependent



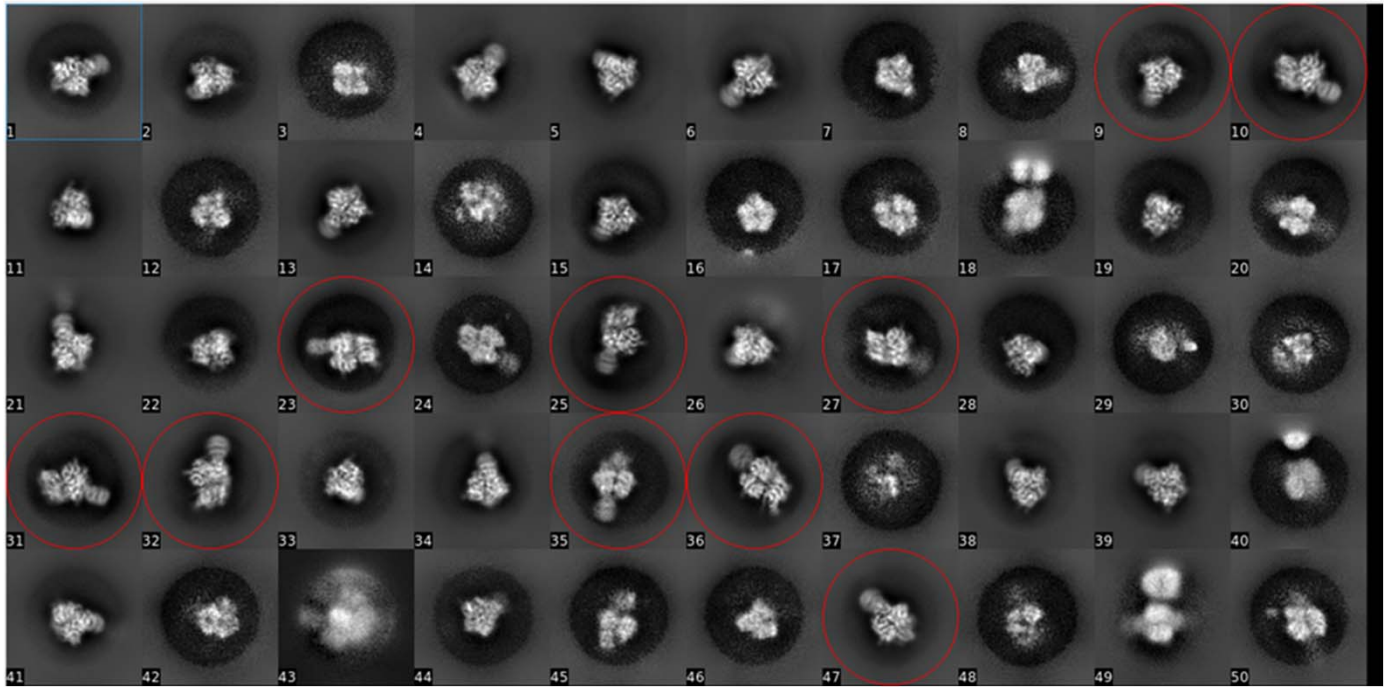
Supplementary Figure 2: Recruitment of RBM39 to DCAF15 is Indisulam-Dependent. 2.5 μ M DCAF15-DDB1(Δ BPB)-DDA1 (DCAF15) was incubated with increasing concentrations of His-ZZ-RBM39(Δ 150) (RBM39) as listed in the legend. The components were subjected to sedimentation velocity in 50 mM HEPES (7.5), 300 mM NaCl & 1 mM TCEP @ 42,000 rpm for 5 h, 20 C. The sedimentation coefficient distribution displays independently migrating His-ZZ-RBM39(Δ 150) (2.7 S) & DCAF15-DDB1(Δ BPB)-DDA1 (6.8 S). In the absence of Indisulam, concentrations as high as 80 μ M His-ZZ-RBM39(Δ 150) do not display a dose-dependent increase the integrated area of a putative DCAF15-DDB1(Δ BPB)-DDA1-RBM39 complex peak or migrate with a higher sedimentation coefficient, inconsistent with the formation of a stable complex in the absence of Indisulam.

Supplementary Figure 3: ^1H -STD Indisulam spectra in the presence and absence of DCAF15-DDB1-DDA1



Supplementary Figure 3: ^1H -STD Indisulam spectra in the presence and absence of DCAF15-DDB1-DDA1. Evidence of binding of Indisulam to DCAF15/DDB1/DDA1: ^1H -1D spectrum of 200 μM Indisulam in the presence of 1 μM DCAF15/DDB1/DDA1 (blue); replicate ^1H -STD spectrum of the same solution (red); ^1H -STD spectrum of a solution containing 200 μM Indisulam, but no protein (black).

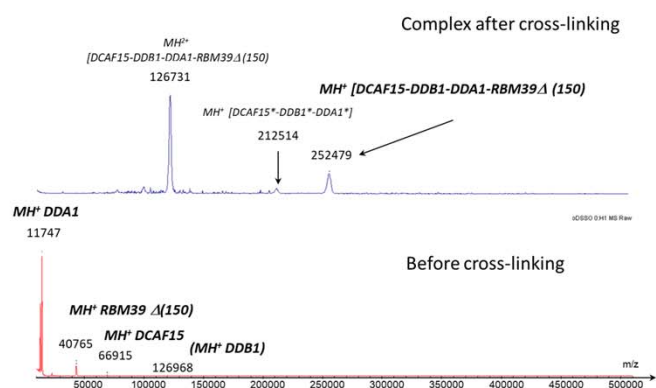
Supplementary Figure 4 : EM 2D-class averages show mixture of DCAF15 ternary complexes and DDB1 alone



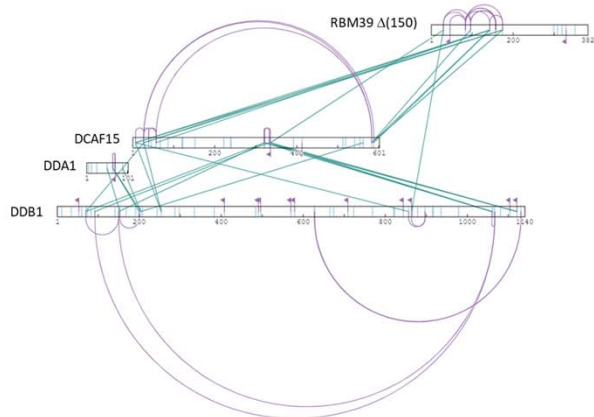
Supplementary Figure 4: EM 2D-class averages show mixture of DCAF15 ternary complexes and DDB1 alone. 2D-class averages showing a mixture of ternary complex and DDB1 alone. For 3D-classification, only ternary complex class, marked with red circle were chosen for further processing.

Supplementary Figure 5: MS crosslinking studies to map DCAF15-DDB1-DDA1-Indisulam-RBM39(Δ 150) interactions

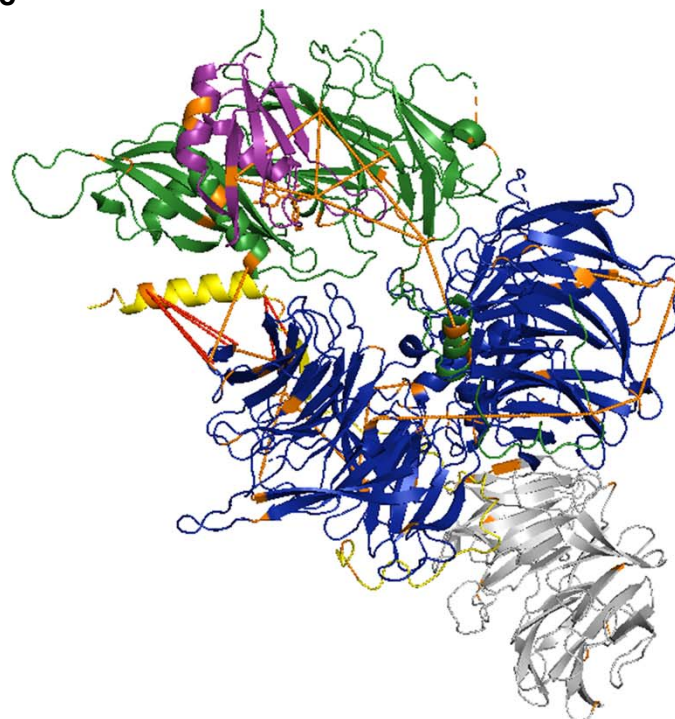
a



b



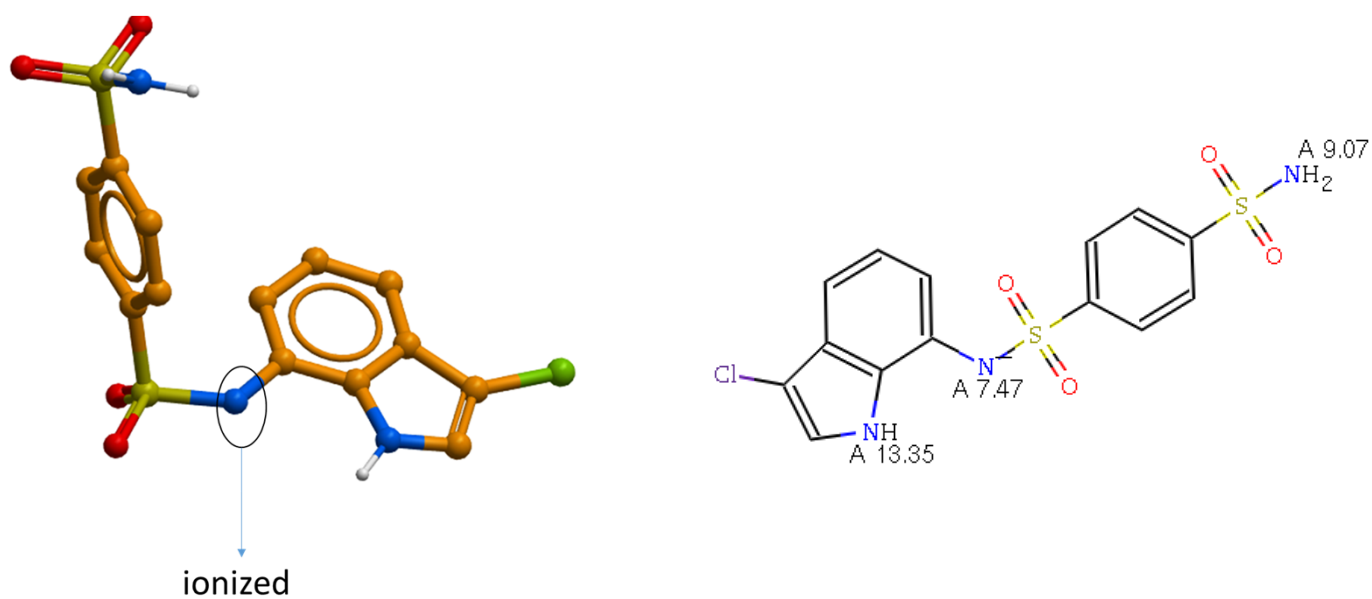
c



Supplementary Figure 5: MS crosslinking studies to map DCAF15-DDB1-DDA1-Indisulam-RBM39(Δ 150) interactions

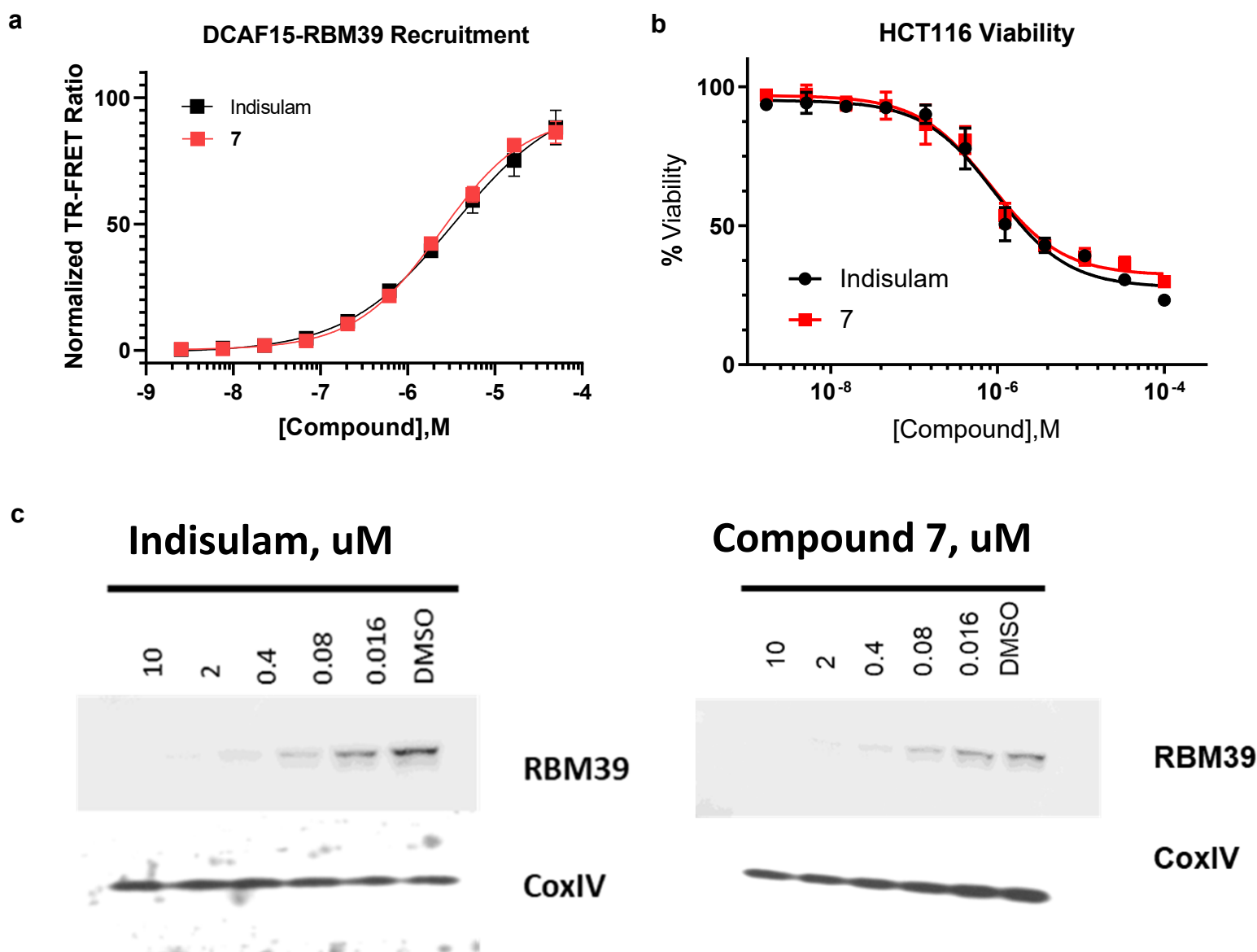
a, MALDI MS spectra of the complex before (bottom) and after (top) the DSSO crosslinking reaction. The major species at 252 kDa confirms the covalent crosslinking of the four protein components with a stoichiometry 1:1:1:1 for DCAF15-DDB1-DDA1-Indisulam-RBM39(Δ 150). **b**, XiNET visualization of the protein-protein interaction mapping within DCAF15-DDB1-DDA1-Indisulam-RBM39(Δ 150): 30 inter-protein (green) and 30 intra- (purple) protein crosslinks were confidently identified. **c**, PyMOL visualization of the cryo-EM structure with the identified inter-protein crosslinks (orange) in the DCAF15-DDB1-DDA1-Indisulam-RBM39(Δ 150) complex. Inter-protein crosslinks in red enabled the determination of DDA1 positioning at the interfaces of DCAF15 and DDB1. Six protein crosslinks were identified between the RBM39 (RRM2) domain and DCAF15. Five protein crosslinks were identified between DDB1 and DDA1 and three of these provided important spatial constraints for the EM model. These three protein crosslinks were between DDB1(Lys153) and DDA1(Lys51), DDB1(Lys200) and DDA1(Lys65), and DDB1(Lys204) and DDA1(Lys65). Two protein crosslinks were identified between the unresolved C-terminal (69-102) of DDA1 and DDB1. Twelve protein crosslinks were also identified to disordered areas of DCAF15, showing interactions between DCAF15 and the N- and C-terminal of DDB1.

Supplementary Figure 6 : Indisulam's DCAF15-bound geometry represents a low energy conformer, assuming an ionized state



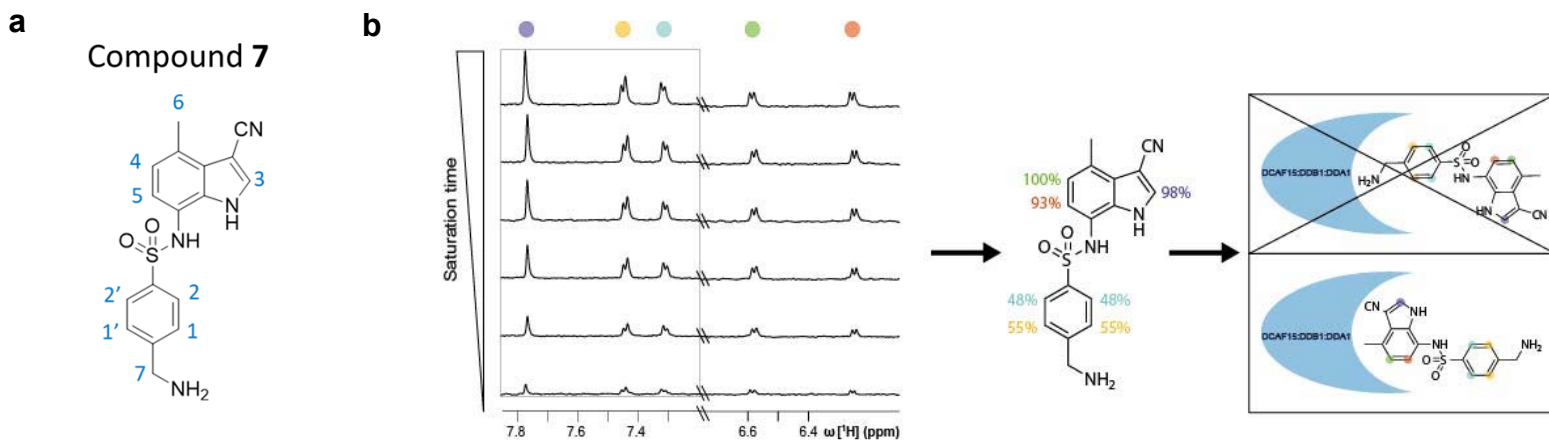
Supplementary Figure 6: Indisulam's DCAF15-bound geometry represents a low energy conformer assuming an ionized state. Predicted pKa value of the sulfonamide nitrogen of Indisulam is 7.47 (MoKa program), suggesting a 50% probability for compound ionization at pH of 7.4. The DCAF15-RBM39-bound geometry of the ionized species predicted by the X-ray structure is a favored low energy conformer.

Supplementary Figure 7: Biochemical and cellular activity of compound 7 on DCAF15-dependent RBM39 recruitment and degradation



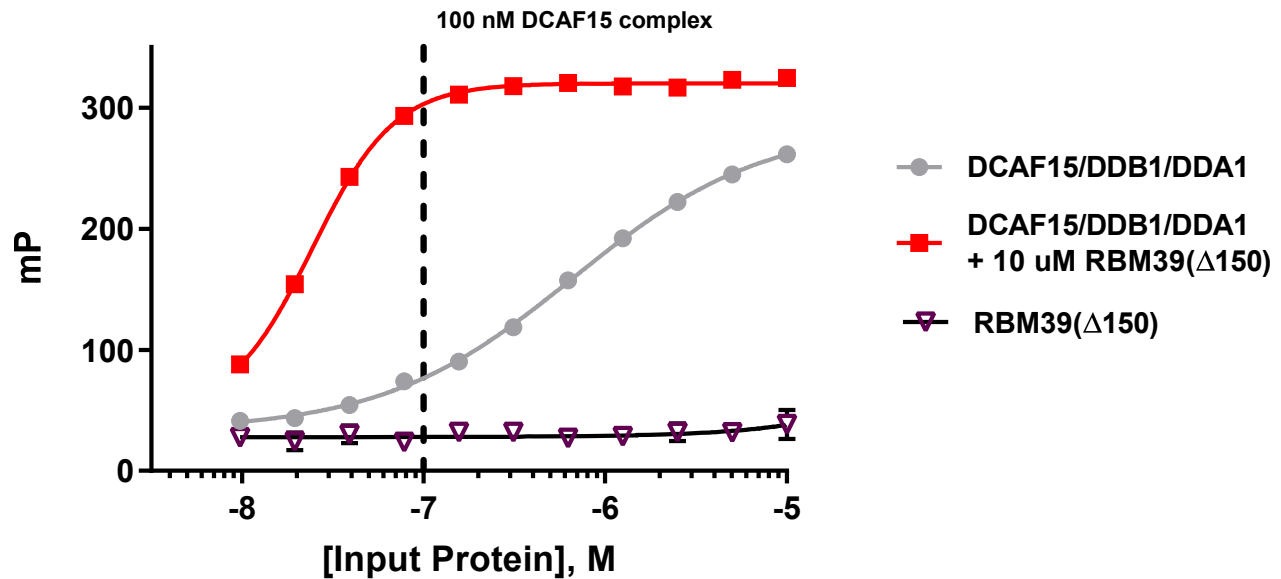
Supplementary Figure 7: Biochemical and cellular activity of compound 7 on DCAF15-dependent RBM39 recruitment and degradation. **a**, Select data from Fig. 5 reproduced for emphasis. DMSO-normalized TR-FRET ratios measured for varied doses of Indisulam (black line) and 7 (red line) in DCAF15-DDB1-DDA1-RBM39 recruitment assay. Error bars represent s.d. of the mean from four biological replicates (n=4) in a single experiment. **b**, Effect of 72 h compound 7 (red line) or Indisulam (black line) treatment on viability (CellTiterGlo) of HCT116 cells. Error bars represent s.d. of the mean from four biological replicates (n=4) in a single experiment. Each experiment was performed two independent times. **c**, Western blots showing levels of RBM39 in HCT116 cells following 6 h treatment of indicated concentrations of Indisulam (left), compound 7(right), or DMSO. Data shown from one individual, representative experiment from two independent repeats.

Supplementary Figure 8 : NMR-based epitope mapping of compound 7 highlights regions in proximity to DCAF15



Supplementary Figure 8: NMR-based epitope mapping of compound 7 highlights regions in proximity to DCAF15. **a**, Structure of the Indisulam analog **7**. **b**, ^1H STD experiments were recorded with different magnetization saturation durations to obtain STD build-up curves (left) which were analyzed to quantify and normalize the amount of magnetization that was transferred from DCAF15-DDB1-DDA1 to each proton in compound **7** (middle). A compound binding model was derived based on the STD results, which show that the protons of the indole receive more magnetization than the ones of the phenyl group and hence, are likely located more closely to the ligase (right).

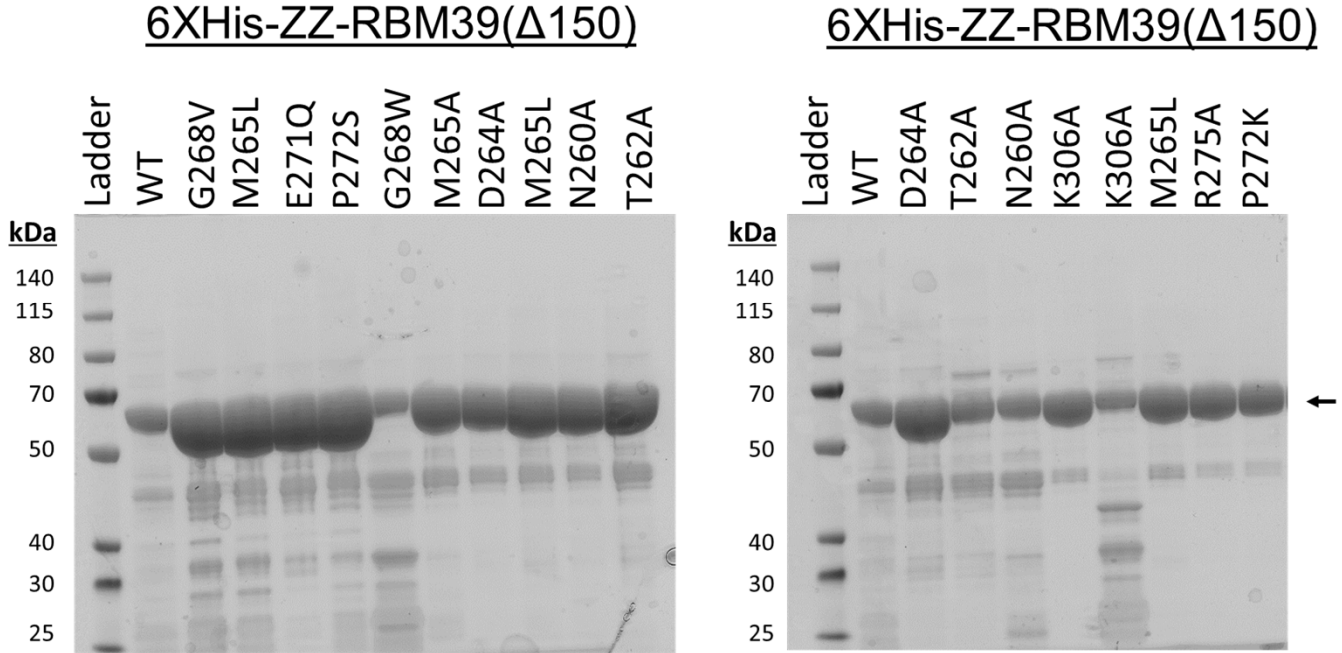
Supplementary Data Figure 9 : DCAF15-DDB1-DDA1 protein titration +/- RBM39(Δ 150) in FP Assay



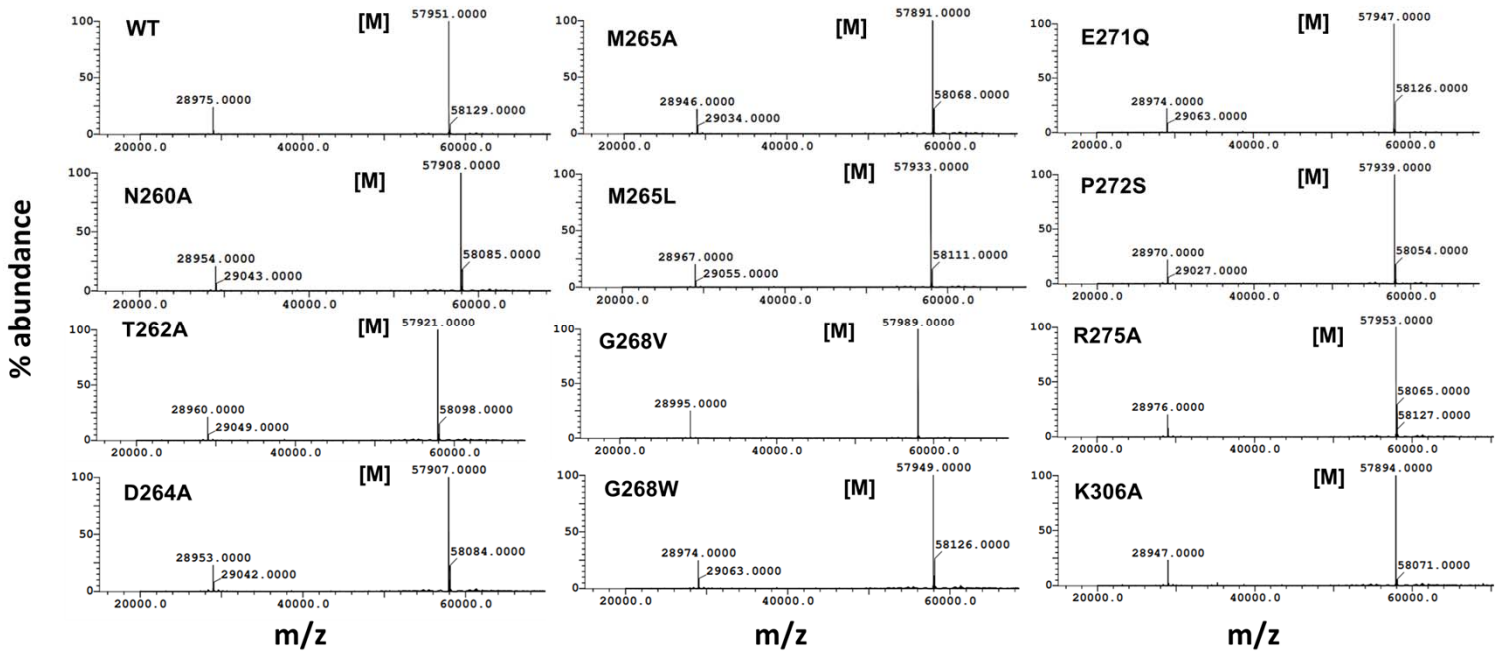
Supplementary Figure 9: DCAF15-DDB1-DDA1 and RBM39 protein titrations in fluorescence polarization assay with compound 9. Fluorescence polarization (FP) measured for 20 nM compound **9**, a FITC-labeled Indisulam analog, following titration of DCAF15-DDB1-DDA1 (grey line) in the presence of 10 μ M RBM39(Δ 150) (red line), DCAF15-DDB1-DDA1 alone (grey line), or RBM39(Δ 150) alone (purple line). While **9** binds DCAF15-DDB1-DDA1 alone, the addition of 10 μ M RBM39(Δ 150) greatly enhances apparent affinity as **9** forms a ternary complex with both proteins. No binding is detected between **9** and RBM39(Δ 150) alone. From these data, low **9** binding occurs at 100 nM DCAF15-DDB1-DDA1, but near maximum binding in the presence of RBM39(Δ 150) at the same concentration (vertical dashed line). As this change in signal reflects enhance binding through ternary complex formation between DCAF15-DDB1-DDA1 and RBM39(Δ 150), These conditions were chosen to assay impact of RBM39(Δ 150) mutation on this phenomenon. Error bars represent s.d. of the mean from four biological replicates (n=8) in a single experiment.

Supplementary Figure 10 : Characterization of purified RBM39 variants

a

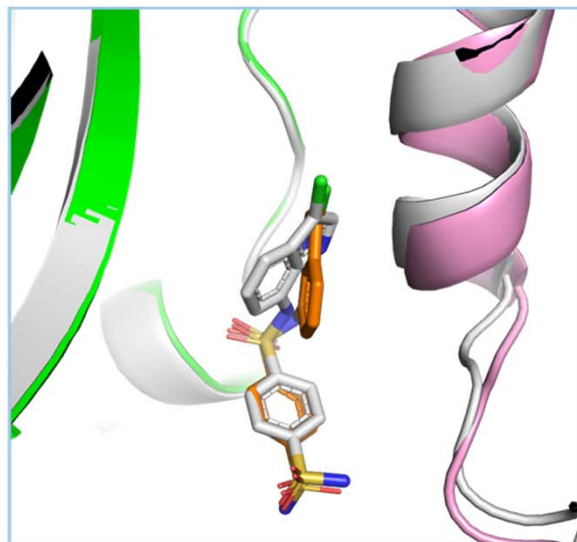


b

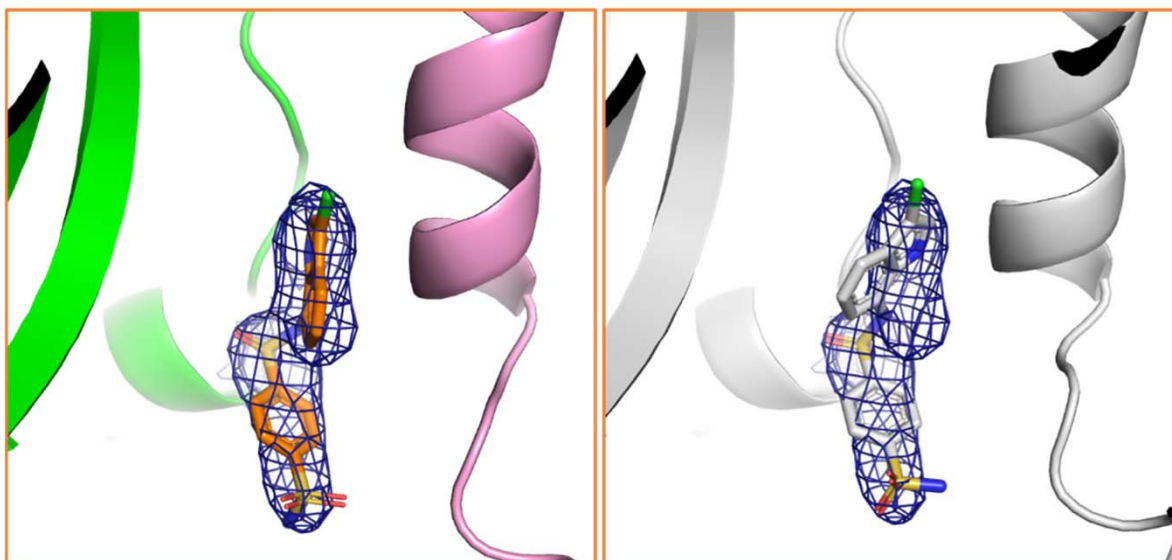


Supplementary Figure 10: Characterization of purified RBM39(Δ 150) variants. a, Coomassie-stained gels of all RBM39(Δ 150) variants used in this study and b, associated LC-MS analysis and mass determination for each prep. Expected mass is represented by [M].

Supplementary Figure 11: Positioning of Indisulam in Cryo-EM and X-ray structures



Superposition of EM- and X-ray coordinates



EM coordinates in EM density

X-ray coordinates in EM density

Supplementary Figure 11: Positioning of Indisulam in Cryo-EM (white) and X-ray (orange) structures. The majority of the Indisulam molecule shows similar conformation (superposition on top), however, the positioning of the chloro-indole group differs by ~30 degrees between Cryo-EM (bottom left) and X-ray (bottom right) structures. The estimated energy of the indisulam binding pose in the EM structure is ~1.4 kcal/mol higher versus the X-ray crystal structure assuming the central sulfonamide is deprotonated. However, due to resolution differences in the data used to fit the compounds, it is likely that the structures are approximately equivalent.

Supplemental discussion

Differences between the structures of the DCAF15-DDB1-DDA1-RBM39(RRM2)-Indisulam complex by X-ray crystallography and cryo-electron microscopy

The orthogonal determination of the co-structure by two separate structural methods allows both the validation of the determined structures as well as an examination of important differences^{1,2}. Generally, the high level of sampling of the macromolecule or macromolecular complex provided by Bragg diffraction coupled with the restriction of movement provided by a three-dimensional crystal matrix allows crystallography to provide higher-resolution data, while the imaging of the macromolecular complex by cryo-EM frozen in vitreous ice allows observation of pertinent dynamics at the cost of some resolution. With the exception of the DDB1-BPB domain, which has been deleted from the crystallographic construct to enforce crystal packing and which cannot be fit in the EM structure due to weak density, the two structures overlap with an RMSD of 1.16 Å between the main-chain atoms of all proteins in the complex, illustrating the high degree of similarity between the two structures (Fig. 2c). However, significant differences do exist. Three loops in DCAF15 which are visible in the crystal structure are not present in the EM structure, and β 12 is also not visible. The trajectory of residues 191-214 differs significantly. The N-terminus and C-terminus of RBM39 diverge between the two structures by 4.45 and 8.18 Å, respectively, while the main body of RBM39 is similar. Several loops present in DDB1 in the crystal structure are not visible in the EM structure. Residues 5-69 of DDA1 are visible in the EM structure, while residues 4-76 are visible in the crystal structure. While most of the rotamers of side-chains are similar between the two structures, there are many cases where the side-chains favor different rotamers. Given the differences in resolution of the two structures, it is difficult to explain these results, as the differences in resolution could affect interpretation of the maps and subsequent refinement of the structure. Some of these differences are likely due to the differences in mobility between the two structures. Some could also be affected by the difference in buffer components and pH between the two systems. Additionally, the crystal structure is necessarily determined in the presence of a chemically complex precipitant solution. In general, as strain is not readily accommodated in a crystal matrix, the crystal structure can be viewed as a low-energy state of the quaternary complex, but

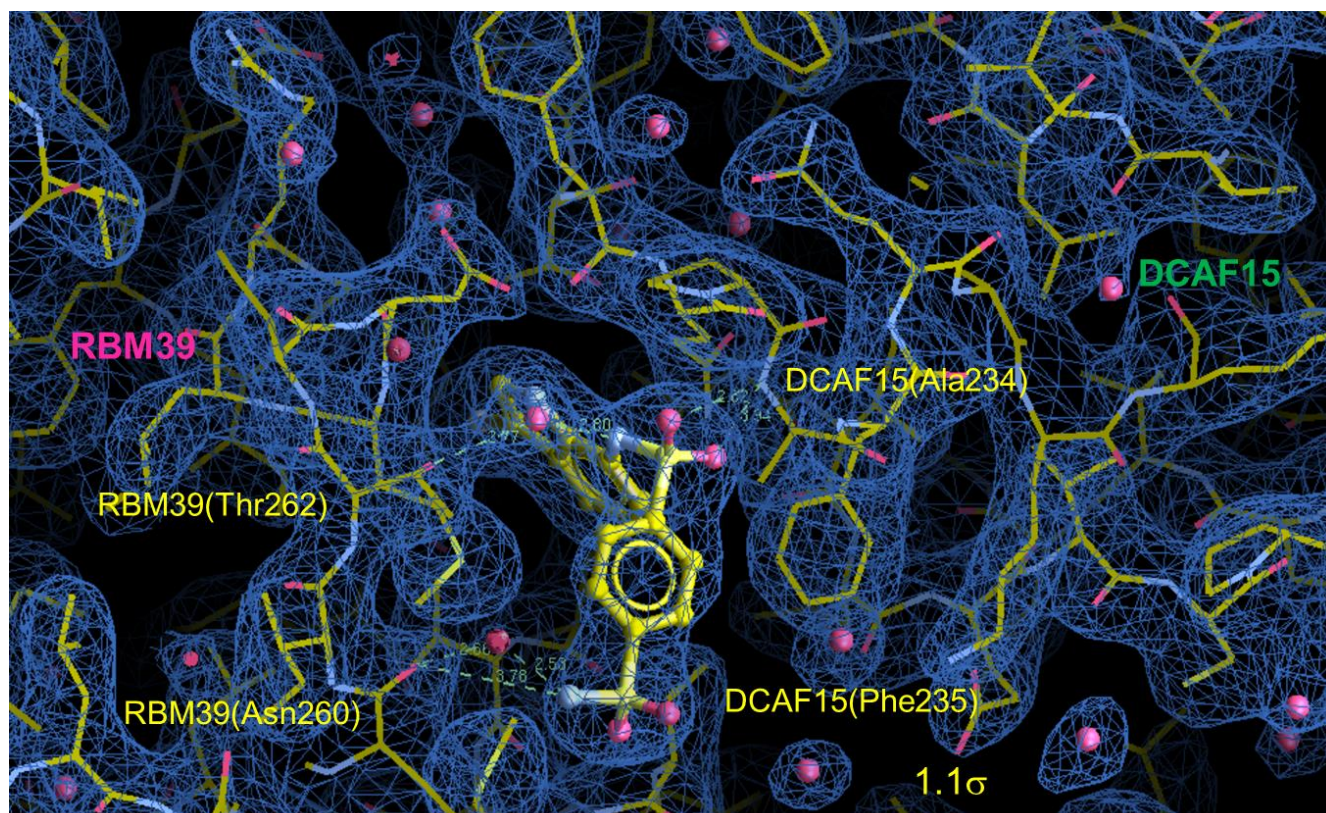
perhaps not the lowest energy state. The cryo-EM structure can be viewed as a representation of the mobility of the complex free in solution, subject, of course, to the freezing process used in cryo-EM.

The Indisulam binding pocket and the binding pose of Indisulam differs slightly between the two structures (Supplementary Fig. 11). While the majority of the compound shows the same conformation, the position of the chloro-indole group differs by approximately 30 degrees within the hydrophobic pocket. Examination of the pocket reveals that the pocket is slightly larger due to a 1.7 Å shift of both Met265 of RBM39 and Met560 of DCAF15 away from the compound, as well as shift in the rotamer of Val556 from DCAF15. This allows the compound to adopt a binding pose with a slightly lower free energy. Calculations (using Gaussian 2009) estimate the energy of the indisulam binding pose in the co-crystal structure to be ~1.4 kcal/mol lower in than the binding pose in the EM structure, assuming that the nitrogen in the central phenylsulfonamide is ionized.

References

1. Wang, H.-W. & Wang, J.-W. How cryo-electron microscopy and X-ray crystallography complement each other. *Protein Sci.* **26**, 32–39 (2017).
2. Vénien-Bryan, C., Li, Z., Vuillard, L. & Boutin, J. A. Cryo-electron microscopy and X-ray crystallography: complementary approaches to structural biology and drug discovery. *Acta Crystallogr. Sect. F Struct. Biol. Commun.* **73**, 174–183 (2017).

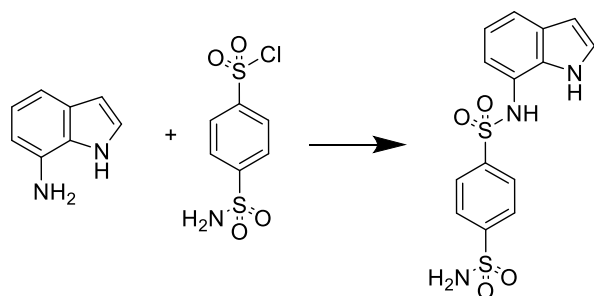
Supplementary Note 1: 2Fo-Fc electron density map for the Indisulam binding pocket and adjacent structure.



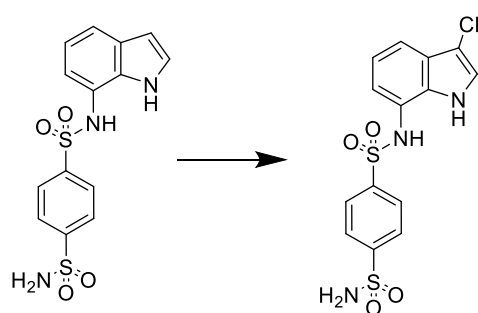
Supplementary Note 1: 2Fo-Fc electron density map for the Indisulam binding pocket and adjacent structure. The map is shown in blue and is contoured at 1.1 σ . Structural waters are shown and key interactions are shown as dotted lines.

Supplementary Note 2: Synthesis of Indisulam and analogs

Indisulam synthesis and characterization



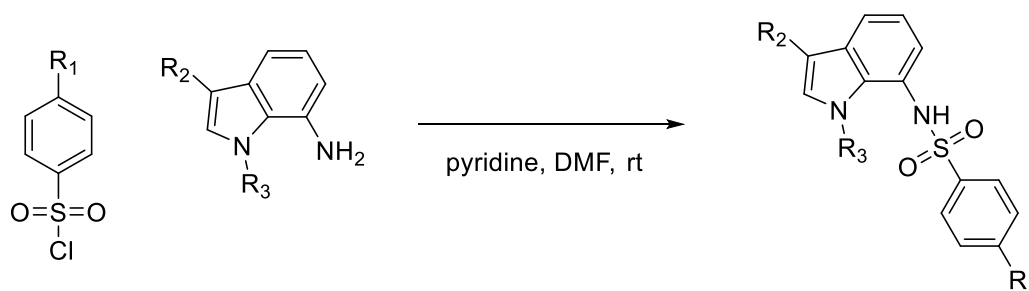
4-sulfamoylbenzene-1-sulfonyl chloride (367 mg, 1.435 mmol) was added to a room temperature solution of 7-aminoindole (187 mg, 1.415 mmol) and pyridine (0.250 mL, 3.09 mmol) in EtOAc (7 mL). The reaction mixture was stirred at room temperature for 2 hrs. The reaction mixture was diluted with EtOAc (30 mL) then washed with 0.5 M HCl (10 mL), sat. aq. NaHCO₃ solution (10 mL), then brine (10 mL). The organic layer was then dried over Na₂SO₄, filtered, loaded onto Celite and purified over SiO₂ column with 0-15% MeOH/DCM to afford N-(1H-indol-7-yl)benzene-1,4-disulfonamide (360mg, 72%). LC-MS: m/z = 352.0297 (M+H⁺); ¹H NMR (400 MHz, DMSO-d₆) δ 10.79 (s, 1H), 10.12 (s, 1H), 7.93 (s, 4H), 7.55 (s, 2H), 7.36 - 7.29 (m, 2H), 6.83 (t, J = 7.7 Hz, 1H), 6.72 - 6.66 (m, 1H), 6.41 (dd, J = 3.0, 2.0 Hz, 1H).



A solution of N-(1H-indol-7-yl)benzene-1,4-disulfonamide (131 mg, 0.373 mmol) in THF (4 mL) was cooled in an ice bath for 10 min. NCS (58mg, 0.42mmol) was then added

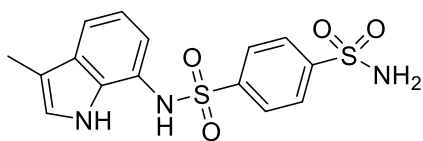
and stirred in the cold bath for 5 min the removed and stirred at room temperature for 1.5 hr. ca. 10% conversion is seen. 1 drop of conc. HCl was then added and stirred at room temperature for 30 min. The reaction mixture was diluted with water (10 mL) and EtOAc (15 mL). The mixture was separated and the aqueous layer was extracted with EtOAc (10 mL). The combined organic layers were then washed with sat. aq. NaHCO₃ solution (10 mL) then brine (10 mL). The organic layer was then dried over Na₂SO₄, filtered, loaded onto celite and purified over SiO₂ with 0-100% EtOAc/heptane to afford Indisulam (93mg, 63%). LC-MS: m/z = 386.0037 (M+H⁺); ¹H NMR (400 MHz, DMSO-d₆) δ 11.10 (s, 1H), 10.21 (s, 1H), 7.97 - 7.90 (m, 4H), 7.56 (s, 2H), 7.50 (d, J = 2.7 Hz, 1H), 7.29 (d, J = 7.9 Hz, 1H), 6.96 (t, J = 7.8 Hz, 1H), 6.76 (d, J = 7.1 Hz, 1H).

General scheme for synthesis of compounds 1, 2, and 4



R₁ = H, SO₂NH₂, SO₂NMe₂, CO₂Me; R₂ = H, Me, CN, Cl; R₃ = H, Me

Synthesis and characterization of compounds 1, 2, and 4

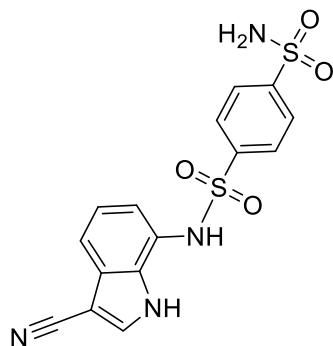


Compound 1 (N-(3-methyl-1H-indol-7-yl)benzene-1,4-disulfonamide)

3-methyl-1H-indol-7-amine (15 mg, 0.103 mmol) was suspended in Pyridine (Volume: 1 mL) and 4-sulfamoylbenzenesulfonyl chloride (34.1 mg, 0.133 mmol) was added. The reaction mixture was stirred at room temp for 16 hrs. Pyridine was removed by vacuo and

redissolved with DMSO. Subjected to prep HPLC and the fractions were lyophilized to yield the desired compound.

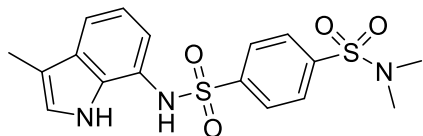
^1H NMR (400 MHz, $\text{DMSO-}d_6$) δ 10.34 (s, 1H), 10.01 (s, 1H), 7.86 (brs, 4H), 7.47 (s, 2H), 7.20 (dt, $J = 7.8, 0.8$ Hz, 1H), 7.02 (dd, $J = 2.5, 1.2$ Hz, 1H), 6.76 (t, $J = 7.7$ Hz, 1H), 6.66 (dd, $J = 7.6, 1.0$ Hz, 1H), 2.13 (s, 3H). LC-MS: m/z 366.4 [M+1].



Compound 2 (*N*-(3-cyano-1H-indol-7-yl)benzene-1,4-disulfonamide)

A mixture of 7-amino-1H-indole-3-carbonitrile (16 mg, 0.102 mmol) and sulphonyl chloride (-, 0.112 mmol) in DMF (Volume: 1 ml, Ratio: 5.00, Total Volume: 6.00 ml) and pyridine (Volume: 0.2 ml, Ratio: 1.000, Total Volume: 1.200 ml) was stirred at RT overnight. The reaction was purified reverse phase HPLC to give the product as off white solids.

^1H NMR (400 MHz, Methanol- d_4) δ 7.99 - 7.96 (m, 2H), 7.96 (s, 1H), 7.83 - 7.78 (m, 2H), 7.52 (dd, $J = 8.0, 0.9$ Hz, 1H), 7.04 (t, $J = 7.8$ Hz, 1H), 6.60 (dd, $J = 7.6, 0.9$ Hz, 1H). LC-MS: m/z 377.1 [M+1].



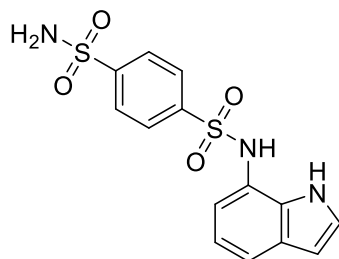
Compound 4 (*N*¹,*N*¹-dimethyl-*N*⁴-(3-methyl-1H-indol-7-yl)benzene-1,4-disulfonamide)

3-methyl-1H-indol-7-amine (10 mg, 0.068 mmol) was dissolved in Pyridine (Volume: 1 mL) and 4-(*N,N*-dimethylsulfamoyl)benzenesulfonyl chloride (23.29 mg, 0.082 mmol) was added. The mixture was stirred for 16hrs. Pyridine was removed and dried. Purified by

silica gel chromatography by using DCM/MeOH to yield final product (13 mg, 0.031 mmol, 45.9 % yield).

^1H NMR (400 MHz, $\text{DMSO-}d_6$) δ 10.25 (s, 1H), 9.97 (s, 1H), 7.87-7.80 (m, 2H), 7.79-7.73 (m, 2H), 7.21 (dt, $J = 7.9, 0.8$ Hz, 1H), 6.97 (dd, $J = 2.5, 1.2$ Hz, 1H), 6.77 (t, $J = 7.7$ Hz, 1H), 6.61 (dd, $J = 7.6, 1.0$ Hz, 1H), 2.49 (s, 6H), 2.11 (s, 3H). LC-MS: m/z 394.2 [M+1].

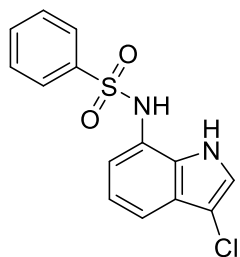
Compound 3 synthesis and characterization



Compound 3 (N-(1H-indol-7-yl)benzene-1,4-disulfonamide)¹⁴

4-sulfamoylbenzene-1-sulfonyl chloride (367 mg, 1.4 mmol) was added to a room temperature solution of 7-aminoindole (187 mg, 1.4 mmol) and pyridine (0.250 mL, 3.09 mmol) in EtOAc (7 mL). The reaction mixture was then stirred at room temperature for 2 hrs. The reaction mixture was diluted with EtOAc (30 mL) then washed with 0.5 M HCl (10 mL), sat. aq. NaHCO_3 solution (10 mL), then brine (10 mL). The organic layer was then dried over Na_2SO_4 , filtered, and concentrated to dryness affording a brown amorphous solid. The solid was then purified by silica gel chromatography, eluting with 0-15% MeOH/DCM, to yield an orange solid. The solid was then triturated with Et₂O/heptane. The mixture was filtered then washed several times with heptane. The solid was then dried under vacuum filtration to afford the desired product as a light pink solid (360 mg, 1.01 mmol, 72% yield). ^1H NMR (400 MHz, $\text{DMSO-}d_6$) δ 10.79 (s, 1H), 10.12 (s, 1H), 7.93 (s, 4H), 7.55 (s, 2H), 7.36 - 7.29 (m, 2H), 6.83 (t, $J = 7.7$ Hz, 1H), 6.72 - 6.66 (m, 1H), 6.41 (dd, $J = 3.0, 2.0$ Hz, 1H). LC-MS: m/z 351.9 [M+H]. HRMS (M+H) calculated $\text{C}_{14}\text{H}_{14}\text{N}_3\text{O}_4\text{S}_2$ 352.0426, found 352.0297.

Compound 5 synthesis and characterization

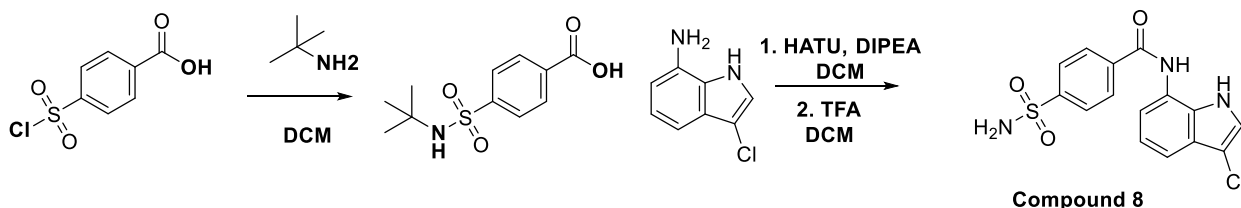


Compound 5 (N-(3-chloro-1H-indol-7-yl)benzenesulfonamide)

Et3N (1.8 mmol) was added to a ca. 0 °C suspension of 3-chloro-1H-indol-7-amine¹⁵ in DCM (10 mL). Benzenesulfonyl chloride (160 mg, 0.9 mmol) was then added and the reaction mixture was allowed to stir and warm up to room temperature overnight. The reaction mixture was quenched with ice water then extracted with DCM (2 X 10 mL). The combined organic layers were washed with water then brine. The organic layer was then dried over Na2SO4, filtered, and concentrated to dryness. The crude material was then purified by silica gel chromatography, eluting with 20-25% EtOAc/hexane, to afford the desired product as a brown solid (28 mg, 0.09 mmol, 10% yield).

¹H NMR (300 MHz, DMSO-d₆): δ 11.01 (s, 1H), 9.99 (s, 1H), 7.74-7.71 (m, 2H), 7.62-7.57 (m, 1H), 7.53-7.46 (m, 3H), 7.24 (d, J = 9 Hz, 1H), 6.94 (t, J = 10 Hz, 1H), 6.77 (d, J = 9.6 Hz, 1H). LC-MS: m/z 305.2 [M-H]

Compound 8 synthesis and characterization



Compound 8 (N-(3-chloro-1H-indol-7-yl)-4-sulfamoylbenzamide)

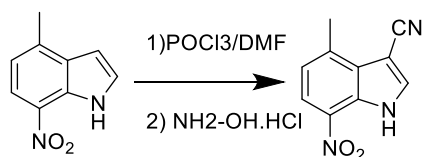
Step 1: To a stirred solution of 4-(chlorosulfonyl)benzoic acid (3g, 13.6 mmol) in DCM (30 mL) was added a solution of tert-butyl amine (5.7 mL, 54 mmol) in DCM (20 mL) at 0 °C. The reaction mixture was allowed to stir and warm up to room temperature over 3 hrs. The reaction mixture was filtered and the solid was washed with DCM then dried under vacuum filtration. The solid was collected then put into water then slowly and carefully acidified to *ca.* pH 3-4 using 5N HCl. The resulting suspension was stirred at room temperature for 20 min then filtered. The solid was washed with water then dried under vacuum filtration to afford the desired 4-(N-(tert-butyl)sulfamoyl)benzoic acid as a white solid (2.5 g, 9.7 mmol, 71% yield). LC-MS: $m/z = 255.9$ [M-H].

Step 2: To a solution of 3-chloro-1H-indol-7-amine¹⁵ (200 mg, 1.2 mmol) in DMF (7 mL) were added 4-(N-(tert-butyl)sulfamoyl)benzoic acid (308 mg, 1.2 mmol), HATU (684 mg, 1.8 mmol), and DIPEA (1.07 mL, 6 mmol). The reaction mixture was then stirred at room temperature for 16 hrs. The reaction mixture was concentrated under reduced pressure to remove DMF and the crude material was purified *via* silica gel chromatography, eluting with 30% EtOAc/heptane, to afford the tert-butyl protected compound 8 as a brown solid (480 mg, 98%). LC-MS: $m/z 406.0$ [M+H].

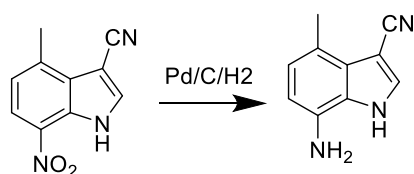
Step 3: To a stirred solution of the brown solid (400 mg, 0.27 mmol) from step 2 in DCM (5 mL) was added TFA (2 mL) at 0 °C. The reaction was then stirred at room temperature for 16 hrs. The reaction mixture was quenched with sat. aq. NaHCO₃ solution then diluted with water. The mixture was extracted with DCM (2 X 10 mL) and the combined organic layers were concentrated to dryness *in vacuo*. The resulting residue was purified by silica gel chromatography, eluting with 70% EtOAc/hexane, to afford the desired COMPOUND 8 as brown solid (20 mg, 0.05 mmol, 19% yield).

¹H NMR (300 MHz, DMSO-d₆): δ 11.2 (br s, 1H), 10.4 (s, 1H), 8.19 (d, $J = 11.6$ Hz, 2H), 7.98 (d, $J = 11.6$ Hz, 2H), 7.56-7.55 (m, 3H), 7.40 (t, $J = 10$ Hz, 2H), 7.14 (t, $J = 10$ Hz, 1H). MS: $m/z 347.9$ [M+H]

Compound 7 synthesis and characterization

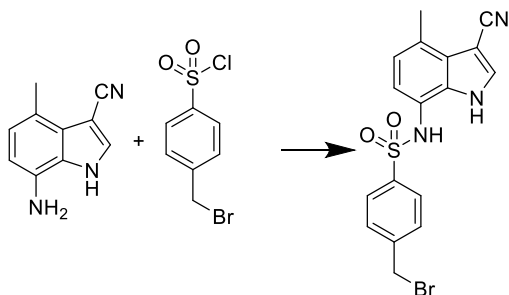


To 1 mL of dimethylformamide was added POCl₃ (0.317 mL, 3.41 mmol) at 0° C., followed by stirring at 0° C. for 0.5 hour. To the reaction mixture was then added a solution of 4-methyl-7-nitro-1H-indole (500 mg, 2.84 mmol) in 2.0ml DMF at 0° C., followed by heating and stirring at 60° C. for 2 hours. To the reaction mixture was then added dropwise a solution of hydroxylamine hydrochloride (394 mg, 5.68 mmol) in 3.0ml DMF with keeping the internal temperature below 80° C., followed by heating and stirring at 60° C. for 40 minutes. The reaction was cooled in an ice bath and 18ml ice water was added to the reaction mixture, which was further stirred 1hr. The precipitated crystals were collected by filtration and washed with water. The crystals were suspended in 18ml H₂O, 1N NaOH was added to the suspension to adjust pH to 7, and then the crystals were collected by filtration, washed with water and dried to afford 4-methyl-7-nitro-1H-indole-3-carbonitrile (520mg, 91%). The crude product was used as it was in the next step. LC-MS m/z = 200.2 (M-H⁺).

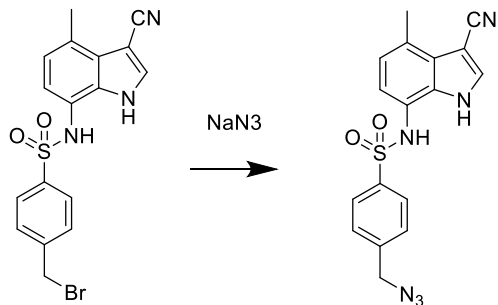


To a solution of 4-methyl-7-nitro-1H-indole-3-carbonitrile (520 mg, 2.58 mmol) in MeOH (Volume: 10 mL, Ratio: 1.000) and THF (Volume: 10 mL, Ratio: 1.000), Pd/C (138 mg, 0.129 mmol) was added. The reaction mixture was treated under H₂ balloon at rt for 2hr. The reaction was filtered and washed with acetone. The filtrated was concentrated to afford 7-amino-4-methyl-1H-indole-3-carbonitrile (443mg, 100%). The crude solid was

used as it was in the next step. LC-MS: $m/z = 170.0$ ($M-H^-$).

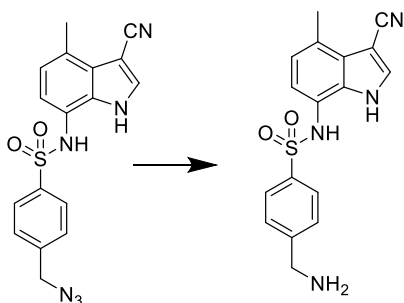


To a solution of 7-amino-4-methyl-1H-indole-3-carbonitrile (300 mg, 1.752 mmol) in THF (Volume: 12 mL) at 0°C, pyridine (0.354 mL, 4.38 mmol) was added. After 10 min. at 0°C, 4-bromomethyl benzenesulphonyl chloride (661 mg, 2.453 mmol) was added. The reaction stirred at rt overnight. The reaction was extracted between H₂O and ethylacetate. Combined all the organics, dried, concentrated and purified over SiO₂ with 40% ethylacetate/heptane to afford 4-(bromomethyl)-N-(3-cyano-4-methyl-1H-indol-7-yl)benzenesulfonamide (250 mg, 35%). LC-MS: $m/z = 402.0$ ($M-H^-$).



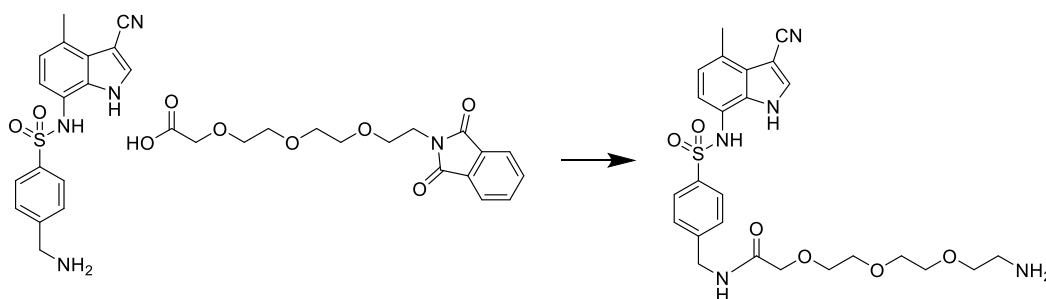
To solution of 4-(bromomethyl)-N-(3-cyano-4-methyl-1H-indol-7-yl)benzenesulfonamide (250 mg, 0.618 mmol) in DMF (Volume: 2 mL), NaN₃ (201 mg, 3.09 mmol) was added, followed by TBAI (45.7 mg, 0.124 mmol). The reaction was treated at 120°C for 0.5 hr under microwave. The reaction was extracted between H₂O and ethylacetate. Combined all the organics, dried, concentrated and purified over SiO₂ with 40% ethylacetate/heptane to afford 4-(azidomethyl)-N-(3-cyano-4-methyl-1H-indol-7-

yl)benzenesulfonamide (200mg, 88%). LC-MS: $m/z = 365.1$ ($M-H^+$).



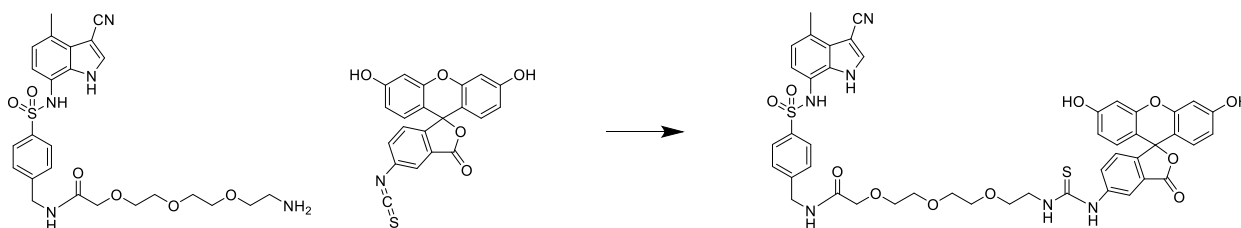
To the solution of 4-(azidomethyl)-N-(3-cyano-4-methyl-1H-indol-7-yl)benzenesulfonamide (680 mg, 1.856 mmol) in THF (Volume: 10 mL, Ratio: 10.00) and H₂O (Volume: 1 mL, Ratio: 1.000), triphenylphosphine (730 mg, 2.78 mmol) was added. The reaction was treated at 60°C for 3hr. The reaction was extracted between H₂O and ethylacetate. All organics were combined, dried, concentrated and purified over SiO₂ with 10% MeOH/DCM to afford 4-(aminomethyl)-N-(3-cyano-4-methyl-1H-indol-7-yl)benzenesulfonamide (500 mg, 79%). LC-MS: $m/z = 341.2$ ($M+H^+$).

Compound 9 synthesis and characterization



To a solution of 4-(aminomethyl)-N-(3-cyano-4-methyl-1H-indol-7-yl)benzenesulfonamide (40 mg, 0.118 mmol) in DMF (Volume: 1.0 mL) at 0 °C, 2-(2-(2-(2-(1,3-dioxisoindolin-2-yl)ethoxy)ethoxy)ethoxy)acetic acid (59.5 mg, 0.176 mmol) and DIPEA (0.051 mL, 0.294 mmol) were added, followed by HATU (89 mg, 0.235 mmol).

The reaction was stirred at 0 °C for 15min. Next, hydrazine (0.037 mL, 1.175 mmol) was added and the reaction was stirred at 50 °C for 0.5hr. The reaction was diluted with DMSO and purified over RP HPLC under basic condition with the detection of the desired product MW to afford 2-(2-(2-(2-aminoethoxy)ethoxy)ethoxy)-N-(4-(N-(3-cyano-4-methyl-1H-indol-7-yl)sulfamoyl)benzyl)acetamide (25mg, 40%). LC-MS: m/z = 530.18 (M+H⁺).



To a solution of 2-(2-(2-(2-aminoethoxy)ethoxy)ethoxy)-N-(4-(N-(3-cyano-4-methyl-1H-indol-7-yl)sulfamoyl)benzyl)acetamide (11 mg, 0.021 mmol) in DMF (Volume: 1.0 mL), FITC (9.70 mg, 0.025 mmol) and DIPEA (10.88 μ l, 0.062 mmol) were added. The reaction was stirred at rt for overnight. The reaction was diluted with DMSO and purified over RP HPLC under acidic condition with UV detection to afford the desired product (15mg, 75%). LC-MS: 919.5 (M+H⁺).